Different Modes of Variability over the Tasman Sea: Implications for Regional Climate*

STEFAN LIESS,[+] ARJUN KUMAR,[#] PETER K. SNYDER,[+] JAYA KAWALE,[#] KARSTEN STEINHAEUSER,[#] FREDERICK H. M. SEMAZZI,[@] AUROOP R. GANGULY,[&] NAGIZA F. SAMATOVA,[**] AND VIPIN KUMAR[#]

[+] *Department of Soil, Water, and Climate, University of Minnesota, Twin Cities, St. Paul, Minnesota*
[#] *Department of Computer Science and Engineering, University of Minnesota, Twin Cities, Minneapolis, Minnesota*
[@] *Department of Marine Earth and Atmospheric Sciences, North Carolina State University, Raleigh, North Carolina*
[&] *Department of Civil and Environmental Engineering, Northeastern University, Boston, Massachusetts*
[**] *Computer Science Department, North Carolina State University, Raleigh, North Carolina*

(Manuscript received 21 November 2013, in final form 19 August 2014)

ABSTRACT

A new approach is used to detect atmospheric teleconnections without being bound by orthogonality (such as empirical orthogonal functions). This method employs negative correlations in a global dataset to detect potential teleconnections. One teleconnection occurs between the Tasman Sea and the Southern Ocean. It is related to El Niño–Southern Oscillation (ENSO), the Indian Ocean dipole (IOD), and the southern annular mode (SAM). This teleconnection is significantly correlated with SAM during austral summer, fall, and winter, with IOD during spring, and with ENSO in summer. It can thus be described as a hybrid between these modes. Given previously found relationships between IOD and ENSO, and IOD's proximity to the teleconnection centers, correlations to IOD are generally stronger than to ENSO.

Increasing pressure over the Tasman Sea leads to higher (lower) surface temperature over eastern Australia (the southwestern Pacific) in all seasons and is related to reduced surface temperature over Wilkes Land and Adélie Land in Antarctica during fall and winter. Precipitation responses are generally negative over New Zealand. For one standard deviation of the teleconnection index, precipitation anomalies are positive over Australia in fall, negative over southern Australia in winter and spring, and negative over eastern Australia in summer. When doubling the threshold, the size of the anomalous high-pressure center increases and annual precipitation anomalies are negative over southeastern Australia and northern New Zealand. Eliassen–Palm fluxes quantify the seasonal dependence of SAM, ENSO, and IOD influences. Analysis of the dynamical interactions between these teleconnection patterns can improve prediction of seasonal temperature and precipitation patterns in Australia and New Zealand.

1. Introduction

Australian climate is influenced by El Niño–Southern Oscillation (ENSO), whereby El Niño conditions inhibit regional rainfall (McBride and Nicholls 1983; Ropelewski and Halpert 1987; Karoly 1989). Given the partial phase synchronization of ENSO with the annual cycle (Stein et al. 2011), the ENSO influence is strongest during austral spring (McBride and Nicholls 1983; Wang and Hendon 2007). However, the ENSO influence on Australian rainfall also varies on a multidecadal time scale (Simmonds and Hope 1997). A decrease in rainfall and an increase in surface temperatures is also related to the negative phase of the southern annular mode (SAM), primarily during austral summer, whereas the negative SAM is associated with increasing rainfall across southern Australia in the cool seasons (L'Heureux and Thompson 2006; Hendon et al. 2007). These oscillation patterns and their regional impacts can be found in monthly-mean data, which filter the large-scale synoptic waves in the troposphere, helping to focus on the nonpropagating component of low-frequency variability (Nigam 2003). The behavior of

* Supplemental information related to this paper is available at the Journals Online website: http://dx.doi.org/10.1175/JCLI-D-13-00713.s1.

Corresponding author address: Stefan Liess, Department of Soil, Water, and Climate, University of Minnesota, Twin Cities, 1991 Upper Buford Circle, St. Paul, MN 55108.
E-mail: liess@umn.edu

DOI: 10.1175/JCLI-D-13-00713.1

these local oscillations can then be used for statistical weather and climate predictions.

In addition to ENSO and SAM, the Indian Ocean dipole (IOD) pattern in sea surface temperature (SST) influences the regional rainfall, especially over Australia (Ummenhofer et al. 2009; Cai et al. 2011c). Atmospheric model simulations for July with increased SST forcing to the northwest of Australia show increases in relative humidity over most of Australia apart from the most southwestern and northeastern regions (Simmonds 1990). This signal is strengthened and a related increase in latent heat flux and precipitation is detectable when the SST to the southwest of Australia is simultaneously decreased, similar to the negative IOD phase (Simmonds and Rocha 1991). The IOD influence on precipitation stretches across the entire Indian Ocean rim region (Cai et al. 2013). This appears to be related to the fact that positive IOD events, when SST anomalies are higher in the western Indian Ocean and lower northwest of Australia, co-occur with El Niño events (Yamagata et al. 2003). However, the IOD activity does not continue into the austral summer because of the arrival of westerly winds with the onset of the Australian monsoon (Cai et al. 2013).

ENSO is also related to the Pacific–South American (PSA) pattern (Mo 2000), and Simmonds and King (2004) provide a detailed analysis of the atmospheric circulation over the Southern Ocean based on ENSO, PSA, and SAM. The present study focuses on the dynamical interplay between SAM, ENSO, and the IOD, and discusses a regional pattern over the Tasman Sea, which is located between the southeastern coast of Australia and Tasmania on the west and New Zealand on the east, and merges with the Coral Sea to the north. The detected teleconnection influences the climate in Australia and New Zealand and is connected to Rossby wave patterns over the Southern Ocean. This teleconnection is correlated to SAM, ENSO, and the IOD during certain seasons, and can thus be considered as a hybrid of these oscillations. In this study, we refer to teleconnections as pairs of regions that are connected via a quasi-stationary wave mechanism and to oscillations as physical modes that show a negative correlation between two regions (including teleconnections). We also use the term ''dipole'' as any result of a search algorithm based on negative correlations, including spurious results and dipoles that are confined to certain seasons.

Cai et al. (2011a) found that SAM leads ENSO by two months in seven-month running-mean data, and ENSO has an influence on SAM whereas SAM has little influence on ENSO. Most of Australia's droughts are related to positive IOD events (Ummenhofer et al. 2009) and El Niños (McBride and Nicholls 1983), but the positive SAM phase is related to drought conditions over southwestern and southeastern Australia during winter in June–August (JJA) (Hendon et al. 2007; Cai et al. 2011b). However, as mentioned above, Hendon et al. (2007) also report increased precipitation during the positive SAM phase over southeastern Australia during September–November (SON) and December–February (DJF). In northeastern Australia, wintertime blocking over the Tasman Sea, which is positively correlated to SAM, contributes to increases in rainfall resulting from stronger southeasterly moisture advection (Klingaman et al. 2013). These blocking situations can occur throughout the year, but have a pronounced peak in winter (Pook et al. 2013; Ummenhofer et al. 2013) when blocking over southeastern Australia is associated with the La Niña phase of ENSO (Cowan et al. 2013). An established blocking index based on 500-hPa zonal wind assumes blocking over 40°–50°S (Wright 1994; Pook and Gibson 1999).

The present study introduces an index based on poleward wave propagation, which assumes blocking occurring within a wider and more equatorward region between 25° and 45°S, and which is accompanied by the opposite wave peak farther south. In this case, the subtropical jet stream weakens, and the polar and subtropical jets can merge to the south of the Tasman Sea and form a strong high-pressure system over the Tasman Sea and a corresponding low pressure system over the Southern Ocean. On the other hand, the established blocking index describes a widening of the gap between the jet streams with the high-pressure system located between the jets (Pook and Gibson 1999). Thus, the established blocking index and the newly introduced index can be negatively correlated when they are located over similar longitudes. However, the blocking index is mostly used around 130°–140°E, whereas the hybrid index over the Tasman Sea is defined around 150°E–180°. The regional SAM pattern and the related meandering polar jet stream can weaken or strengthen these indices based on their longitudes.

The influence of SAM on Australian rainfall is weakest during March–May (MAM) (Hendon et al. 2007; Klingaman et al. 2013), and also the ENSO influence is not a reliable predictor during MAM, when the grain-growing season starts in southeastern Australia (Pook et al. 2009) and winter wheat is planted in Queensland (McIntosh et al. 2005). However, the teleconnection identified in this study indicates a statistically significant relationship to MAM rainfall over the most densely populated Australian states of New South Wales and Victoria, and the Auckland region in New Zealand, with a combined population of about 14 million inhabitants.

Traditionally, atmospheric oscillations have been identified by analyzing correlations between station data (e.g., Walker and Bliss 1932; Hurrell 1995), correlations within gridded datasets (e.g., Wallace and Gutzler 1981), with empirical orthogonal functions (EOFs; e.g., Barnston and Livezey 1987), and with empirical orthogonal teleconnections (EOTs; van den Dool et al. 2000). EOTs either find the point in space that explains most of the variance of all points or find the time step that explains most of the variance of all time steps. After this first point is either found automatically or specified by the user, all other points can be sorted by the remaining explained variance over a fixed domain. This results in a set of orthogonal patterns in either time or space. In the former setup, the difference with respect to EOFs is that the initial time series is taken at one specific grid point rather than a more general linear combination over space. Nigam (2003) provides an overview of existing techniques for the detection of atmospheric teleconnection behavior. Klingaman et al. (2013) used EOTs of rainfall to detect relevant circulation patterns such as the ENSO influence on northern Queensland rainfall during JJA, SON, and DJF. Here, we use a novel approach based on shared reciprocal nearest neighbors (SRNN; Kawale et al. 2013). Apart from monthly-mean data, we also analyze subdaily eddy propagation, which is necessary to explain the initiation of teleconnections (Nigam 2003).

2. Detection of hybrid teleconnections

An SRNN approach (Kawale et al. 2013) is applied to global monthly-mean Hadley Centre sea level pressure (SLP) anomalies (HadSLP2; Allan and Ansell 2006) and to Modern Era-Retrospective Analysis for Research and Applications (MERRA) SLP (Rienecker et al. 2011) to identify oscillations based on negative correlations. The relatively short 33-yr period from 1979 to 2011 is selected for analysis because of limited observations in earlier periods over the southern high latitudes. For this analysis, monthly SLP anomalies were computed and detrended over the analysis time period, then normalized with their standard deviation to account for the stronger variability over high and midlatitudes compared to low latitudes (Gillett and Stott 2009).

Most studies of teleconnection patterns use data from middle or upper tropospheric levels where the signal appears to be less influenced by surface friction. However, the SRNN approach identifies strong signals in SLP, which might be more valuable for synopticians when diagnosing the atmospheric circulation, because it reflects a vertical integration of the whole atmospheric structure and it incorporates a more direct relation to surface temperature and the low-level convergence required for both deep and shallow convection to initiate precipitation (Trenberth and Caron 2000; Simmonds 2003).

The SRNN approach follows a graph-based methodology (Steinbach et al. 2003; Tsonis et al. 2006). For each grid point n, the k most strongly positive and negative correlated grid points are identified as its positive and negative neighbors. If k is much larger than the expected gridpoint size of a region that can serve as one end of an oscillation, small dipole regions can remain undetected. We use $k = 25$ and empirical results indicate that the approach is robust to variations in k within a reasonable range (Kawale et al. 2013). Positive and negative neighbor lists, or graphs, are constructed by retaining only connections that are mutual (i.e., grid point A is one of the k nearest neighbors of B and vice versa). In these positive and negative shared nearest neighbor graphs, connections between two grid points are weighted by the number of shared neighbors. The positive and negative graphs are then combined by multiplying their weights to derive the SRNN graph. The density of each location is defined as the sum of weights. Contiguous regions of high density are calculated using a clustering algorithm. The correlation of every cluster pair is computed and negative correlations between clusters indicate dipoles. The strength of these dipoles is measured by the strength of the correlation.

The SRNN approach can identify both strong and weak dipoles simultaneously, and all major teleconnections were consistently identified in multiple reanalysis products (Kawale et al. 2013, their Fig. 14). However, the clustering algorithm can limit the spatial extent of the detected contiguous regions, and as with any other purely statistical method, the SRNN method depends on the time window of the input dataset, because dipoles can change over time. Since it can also detect many spurious dipoles, its results require a physics-guided analysis to explain the observed behavior.

The SRNN method enables detection of multiple teleconnections of similar strengths without requiring a priori region selection or imposing an orthogonality constraint, as in EOF analysis (Dommenget and Latif 2002). After detecting the first EOF, the following EOFs are dependent on the selection of this detection. Although this constraint can be reduced by rotating EOFs within the search space, the SRNN approach produces very similar results for global datasets or their spatial subsets and is only dependent on the number of nearest neighbors within the search space. The SRNN approach can find many nonorthogonal modes in a region of interest. It does not require a maximum variance criterion.

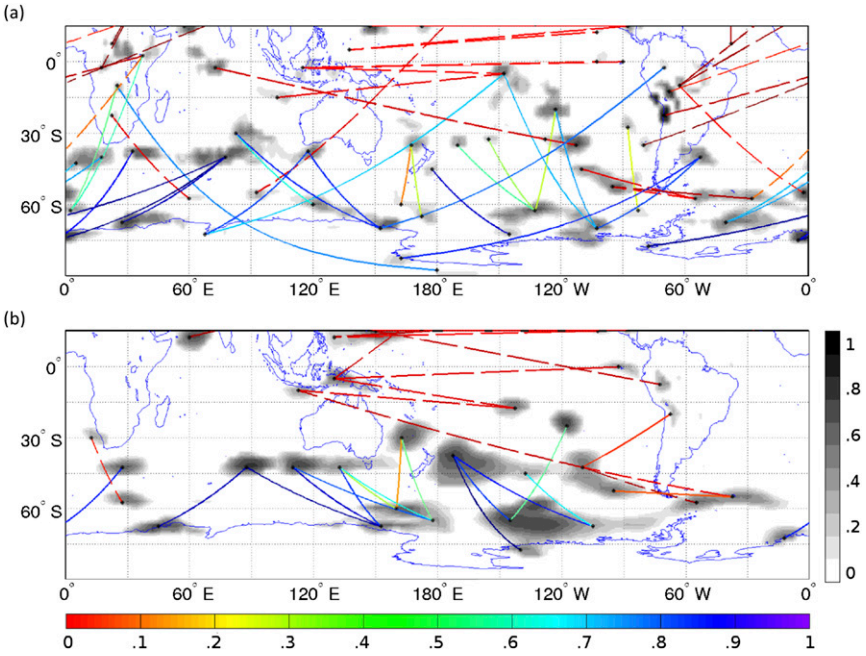

FIG. 1. Network of dipole patterns for 1979–2011 based on SRNN method in (a) HadSLP2 and (b) MERRA SLP with normalized connection weights (gray shading) and correlation of each weighted area averaged time series with the SAM index (color shading). Dashed lines indicate no statistical significance at the 95% confidence interval.

The statistical significance of each mode can be tested by determining the correlation between the two end points and the effective degrees of freedom of this correlation. As in Meneghini et al. (2007), the actual effective degrees of freedom for each correlation are chosen here by selecting the smaller value of the effective degrees of freedom of each of the two time series.

Figure 1 shows the network of all detected statistically significant connections over the Southern Hemisphere for HadSLP2 and MERRA SLP, both interpolated to 2.5° × 2.5°. The SRNN analysis detects the SAM and ENSO patterns; however, the HadSLP2 dataset shows more spurious dipoles than the MERRA reanalysis. Line coloring indicates the absolute correlation of each connection (the time series of the difference between both centers) with the monthly SAM index, which is provided by the Climate Prediction Center (CPC) as the Antarctic Oscillation (AAO) index (AOI). Dashed lines indicate no significant correlation to SAM. The lowest correlations can be found for the PSA, a stationary wave related to upwelling in the Benguela Current (Goubanova et al. 2013), and the distinct teleconnection between the Tasman Sea and the Southern Ocean. The latter is similar to the third EOF over the Southern Hemisphere in the National Centers for Environmental Prediction (NCEP) and European Centre for Medium-Range Weather Forecasts (ECMWF) reanalyses (Mo 2000, her Figs. 1c and 1f). However, we suggest that SRNN can detect these regional patterns without being influenced by large-scale loading patterns as in EOF analysis.

3. Regional characteristics

The polygons in Fig. 2 depict the extent of the northern (north of 45°S) and southern (south of 45°S) centers of the identified teleconnection in the Tasman Sea and the Southern Ocean based on HadSLP2. Results from MERRA SLP are very similar (not shown). Color coding illustrates the annual and seasonal patterns. The overlapping locations indicate only limited seasonal north–south propagation of the centers of action. This is related to very little change of transient eddies in the Southern Hemisphere with the seasons (Trenberth 1981). The northern center is located farthest southeast during MAM, reaching closest to New Zealand, whereas the southern center is located farthest west during DJF. Table 1 lists the correlation of the area-averaged HadSLP2 time series over the northern and southern annual and seasonal centers (see Fig. 2) to the SAM index, the Niño-3.4 SST anomalies, and the dipole mode index (DMI). The new hybrid teleconnection (HT) is defined by the HT index (HTI), which comprises the time series of the northern minus southern centers,

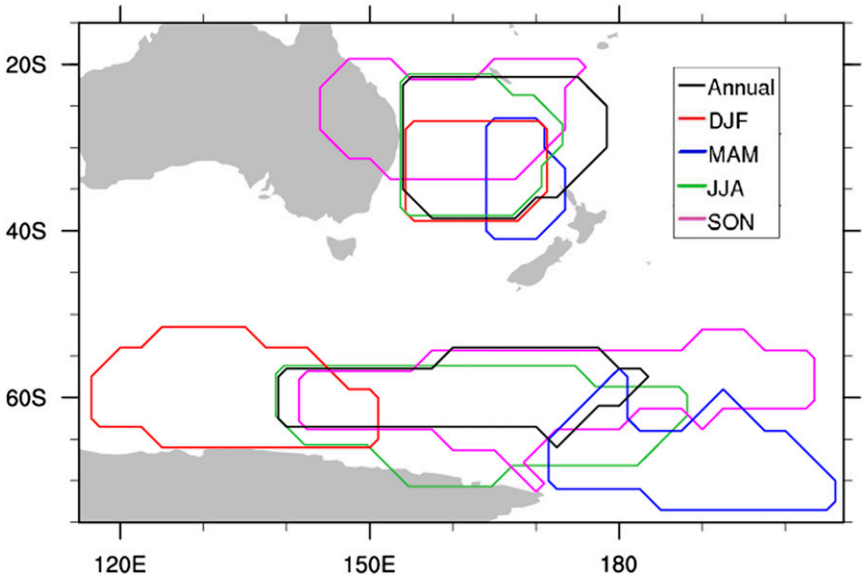

FIG. 2. Northern and southern centers (north and south of 45°S, respectively) of the hybrid teleconnection using the SRNN approach for each of the four seasons and annually.

$$\mathrm{HTI} = \left\{ \frac{\mathrm{detrend(SLPA}_N)}{\sigma_{\mathrm{detrend(SLPA}_N)}} \right\} - \left\{ \frac{\mathrm{detrend(SLPA}_S)}{\sigma_{\mathrm{detrend(SLPA}_S)}} \right\} \quad (1)$$

where SLPA_N and SLPA_S are the multiyear monthly-mean SLP anomalies for all grid points over the northern and southern centers, respectively; σ indicates their standard deviation and curly brackets denote the weighted area average over all grid points in each center. In this study, we use the seasonal centers for seasonal analysis and annual centers for annual analysis. However, the difference is negligible because of the overlapping regions. Even the wider spacing of the southern centers during DJF and MAM has only a minimal effect because of the low zonal wavenumbers for monthly-mean values in the Antarctic Circumpolar Current (ACC) region around 60°S (e.g., Nowlin and Klinck 1986).

Monthly SAM indices and Niño-3.4 SST anomalies are provided by CPC. The IOD is described by the DMI, which is based on the Hadley Centre Sea Ice and Sea Surface Temperature (HadISST) dataset. It is made available by the Japan Agency for Marine-Earth Science and Technology (JAMSTEC; http://www.jamstec.go.jp/frcgc/research/d1/iod/DATA/dmi_HadISST_jan1958-dec2012.txt). Also included in Table 1 are monthly values of the SLP-based regional Antarctic Oscillation index (AOIR) introduced by Meneghini et al. (2007). This index focuses on the wider Australian region between 90°E and 180°, and is thus more strongly correlated to the HTI than the hemispheric SAM index. However, the wider longitudinal coverage of 90° for AOIR compared to about 30° for the HTI smooths the signal of individual wave peaks.

Autocorrelation is taken into account for the statistical significance of all correlations by adjusting the degrees of freedom based on Meneghini et al. (2007) as

TABLE 1. Correlation of hybrid teleconnection index, and time series of northern and southern centers to SAM, AOIR, ENSO, and IOD as defined by area averages of the polygons in Fig. 1. Boldface values represent significance at 95%. N/A indicates data is not available.

	Index				Northern end				Southern end			
	SAM	AOIR	Niño-3.4	DMI	SAM	AOIR	Niño-3.4	DMI	SAM	AOIR	Niño-3.4	DMI
Annual	**0.20**	**0.56**	0.23	0.22	**0.14**	**0.49**	0.25	**0.28**	**−0.18**	**−0.40**	−0.11	−0.08
DJF	**0.22**	**0.56**	**0.26**	N/A	−0.01	**0.42**	**0.46**	N/A	**−0.37**	**−0.47**	0.06	N/A
MAM	**0.23**	**0.54**	0.03	N/A	0.10	**0.46**	0.07	N/A	**−0.30**	**−0.43**	0.03	N/A
JJA	**0.53**	**0.79**	0.06	0.21	**0.37**	**0.66**	0.07	0.31	**−0.55**	**−0.69**	−0.03	−0.04
SON	−0.01	**0.43**	0.31	**0.34**	0.02	**0.49**	0.34	**0.37**	0.04	**−0.24**	−0.17	−0.20

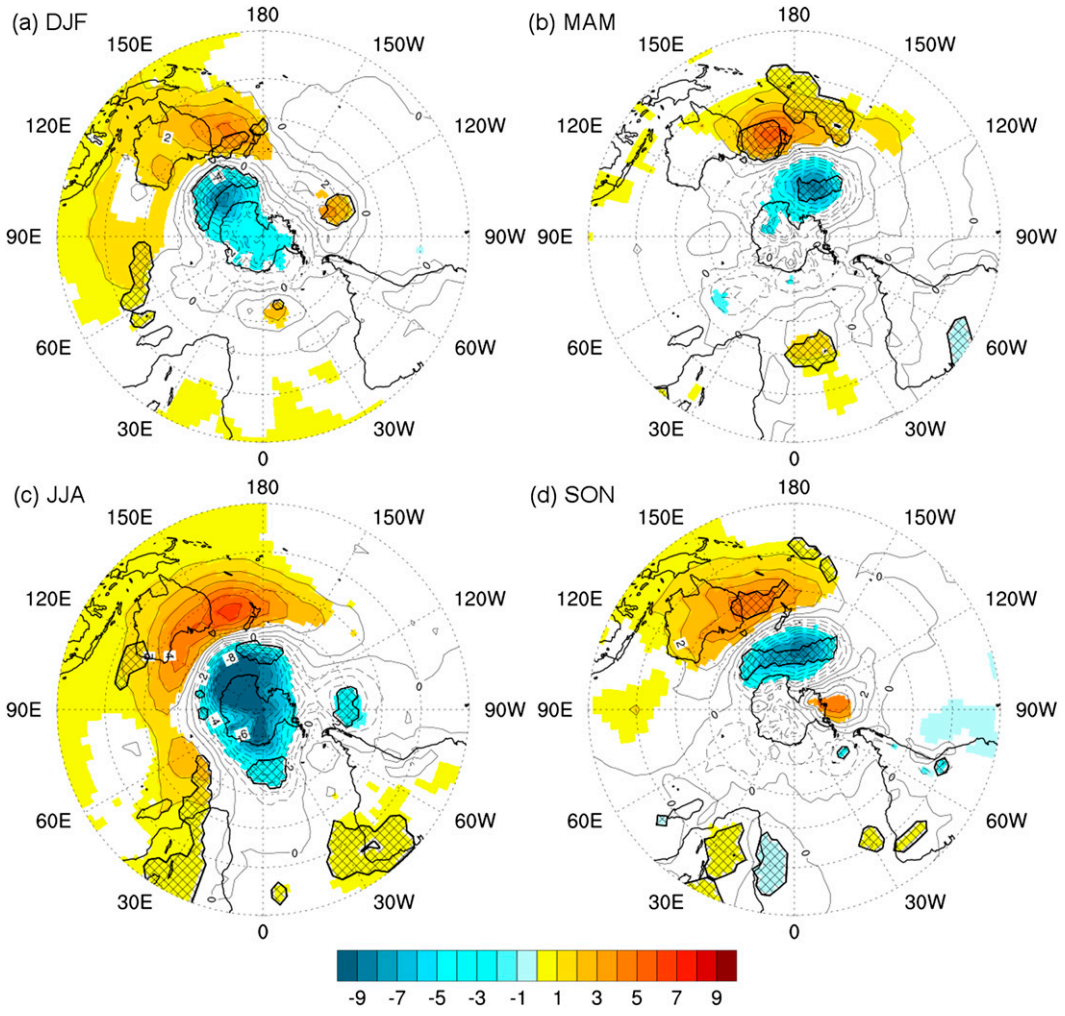

FIG. 3. HadSLP2 composites (hPa) between positive and negative HT phases during four seasons. Shading indicates significance using a *t* test at a 95% confidence level. Hatching represents areas that are significant for the HT but not for SAM, ENSO, or IOD. Latitude intervals are 15° from equator to pole.

outlined in section 2. However, it should be noted that statistical significance does not necessarily indicate causal relationships. Thus, in this study, we have excluded the DMI analysis for DJF and MAM, when the IOD is inactive (Cai et al. 2013).

The southern center of the HT is partly related to SAM, especially during DJF, MAM, and JJA, whereas the northern center is correlated to the ENSO cycle in southern summer (DJF). The northern center is modified by ENSO and is related to variations in the eddy momentum flux during this season (L'Heureux and Thompson 2006). Generally, stronger correlations to DMI versus ENSO are due to the closer spatial proximity of both IOD locations compared to the more distant Niño-3.4 region bounded by 5°N–5°S, 170°–120°W. It should be noted that the SST-based indices for ENSO and IOD used in this study are smoother and thus have largely reduced effective degrees of freedom. In contrast to the 2-month lag of EOF-based ENSO to SAM in mean SLP, as found in 7-monthly smoothed data (Cai et al. 2011a), lag correlations in nonsmoothed SAM and ENSO indices from CPC (based on 700-hPa geopotential height and Niño-3.4 SST, respectively) do not indicate a significant lag relationship between these indices. Also, the HTI shows no significant lag relationship to the SAM and ENSO indices used here (not shown). The SAM exists as a more uniform pattern in the 700-hPa geopotential height field compared to the SLP-based index of Marshall (2003).

The composite maps of SLP for each season (Fig. 3) are derived by selecting months with HTI amplitudes larger than one standard deviation. The number of

TABLE 2. Strength of the teleconnection for HadSLP2, MERRA SLP, and different MERRA geopotential heights based on the two hybrid centers. Boldface values represent significance at 95%.

	HadSLP2	MERRA SLP	700 hPa	500 hPa	300 hPa	200 hPa	150 hPa	100 hPa	50 hPa
Annual	**−0.29**	**−0.42**	**−0.46**	**−0.43**	**−0.40**	**−0.38**	**−0.33**	**−0.26**	−0.06
DJF	−0.24	−0.26	−0.39	**−0.44**	**−0.44**	**−0.40**	−0.36	−0.31	0.09
MAM	**−0.29**	**−0.40**	**−0.48**	**−0.50**	**−0.48**	**−0.49**	**−0.50**	**−0.51**	**−0.32**
JJA	**−0.44**	**−0.61**	**−0.64**	**−0.59**	**−0.52**	**−0.48**	**−0.41**	−0.30	−0.12
SON	**−0.46**	**−0.51**	**−0.52**	**−0.42**	**−0.41**	**−0.43**	−0.34	−0.33	−0.21

months included for the positive (negative) phase from each season is 12 (14) for DJF, 11 (13) for MAM, 17 (14) for JJA, and 12 (15) for SON. Significant differences between the positive and negative phase are identified with a Student's *t* test at a 95% confidence interval (shaded in Fig. 3). Composite maps were also generated for the SAM, ENSO, and IOD patterns (see Figs. S1–S3 in the supplemental material). Regions where only the impact of the HT is statistically significant are hatched in Fig. 3.

Despite the statistically significant correlations between the HT and the general SAM, ENSO, and IOD patterns, the regional centers over the Tasman Sea and the Southern Ocean are only included in the statistically significant composite patterns of the HT and not in the SAM, ENSO, and IOD patterns during most of the year (hatched regions). For southern winter, when the HT is related to SAM and IOD (indicated by absence of hatching over both centers in Fig. 3c), Matthewman and Magnusdottir (2012) found a similar stationary teleconnection pattern in their detailed analysis of transient and stationary eddies (their Fig. 5c). Figure 3c shows wintertime blocking over the Tasman Sea related to IOD and SAM (see Figs. S2 and S3 in the supplemental material). However, the local peak over the Tasman Sea described by the HT is located farther north between 30° and 40°S compared to 45°S for IOD and SAM influences, and has a stronger amplitude over this region. This blocking can increase rainfall in eastern Australia due to stronger easterly moisture advection (Klingaman et al. 2013).

To characterize the vertical extent of the teleconnection signal through the troposphere and lower stratosphere, Table 2 lists the correlations between the two centers for HadSLP2 as well as SLP and geopotential height from MERRA at various pressure levels. Since HadSLP2 relies on limited observations in this region, temporal correlations may be lower than those in MERRA. The interplay between SAM and ENSO forms the detected signal throughout the troposphere, with the largest correlation values of −0.61 and −0.64 in the MERRA reanalysis found near the surface and 700 hPa during JJA, when SLP at the northern (southern) center is correlated at 0.37 (−0.55) with the SAM (see Table 1). This indicates that the detected signal is part of the SAM during this season. However, during SON, when the teleconnection is still strong with a correlation of −0.51, the index and its northern center are correlated to IOD with values of 0.34 and 0.37, respectively, whereas no significant correlation to SAM and ENSO exists. During the DJF wet season over northern Australia, a significant correlation of −0.44 occurs between the two centers around 500 hPa, when SLP at the northern center is correlated at 0.46 with ENSO and at the southern center at −0.37 with SAM. During MAM, SAM influences the HT, shown by a significant correlation of −0.30 (0.23) between the southern center (index) and SAM. The correlation between the HT centers is significant throughout the troposphere and lower stratosphere during MAM.

The comparison of SLP composites (Fig. 3) with 300-hPa geopotential height composites (Fig. 4) shows a westward tilt with height related to poleward heat transport, especially for the northern center over the Tasman Sea in SLP, which is closer to Tasmania in 300-hPa geopotential height. For all seasons, the teleconnection signal is independent of ENSO, SAM, and IOD over larger regions than in SLP composites (see also Figs. S4–S6 in the supplemental material). As shown in Fig. 2, the northern center is located farther east during MAM, when it is mostly independent of the ENSO and SAM signals over most of Australia and New Zealand. The composite of 50-hPa geopotential height anomalies (Fig. 5) suggests a similar teleconnection pattern in the lower stratosphere during MAM and JJA. The northern center is missing in SON, and the southern center is not significant in DJF.

These geopotential height anomalies indicate a vertically coherent zonal wind anomaly pattern that can extend from Earth's surface upward into the lower stratosphere. At 50 hPa, the strongest positive geopotential height anomalies are found north of the Ross Sea and Bellingshausen Sea during DJF and MAM. These anomalies might be precursors for the tripolar pattern in MAM and the HT pattern in JJA, when an insignificant positive geopotential height anomaly remains over the Falkland Islands. However, the polar vortex is strongest in midwinter

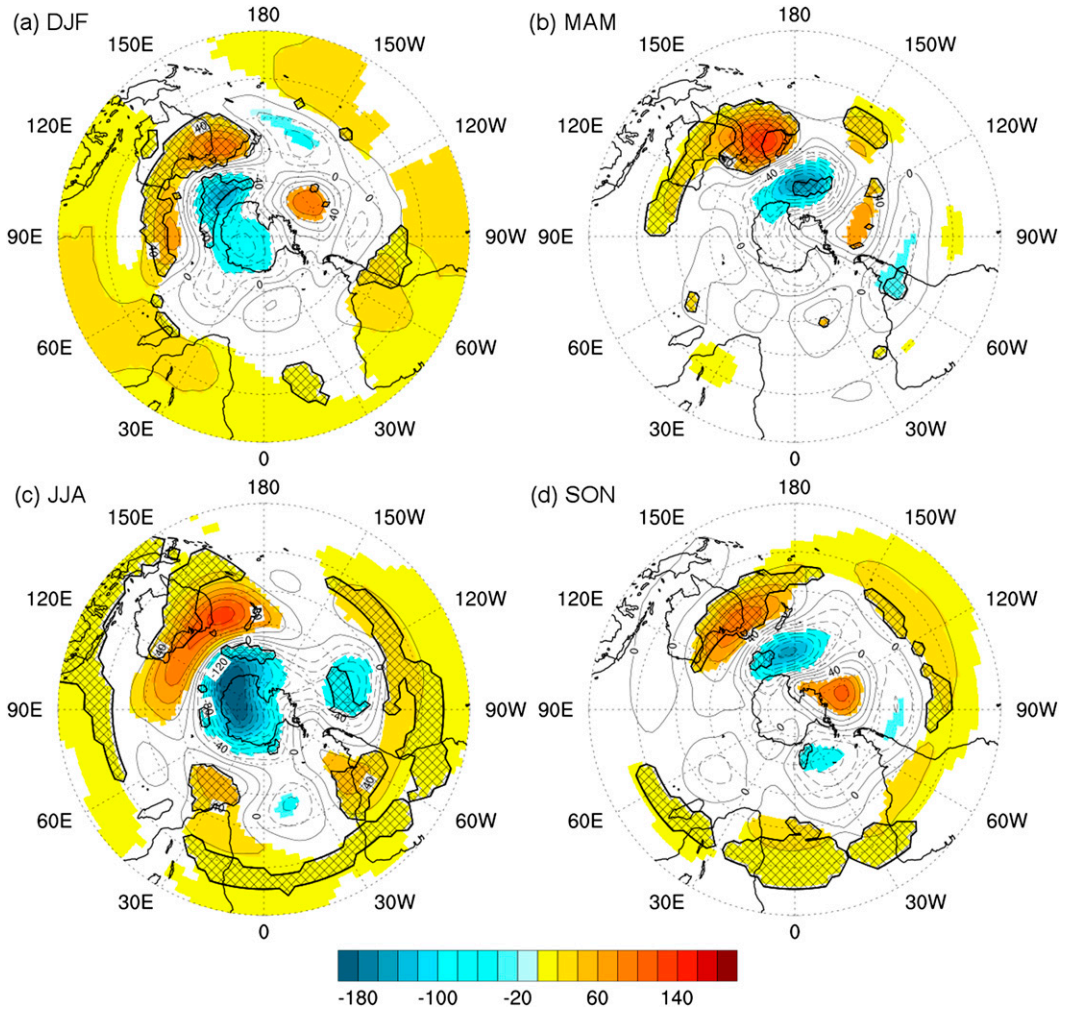

FIG. 4. As in Fig. 3, but for 300-hPa geopotential height (m).

and thus is less prone to zonal anomalies in geopotential height.

The significant correlation at 50 hPa during MAM (see Table 2) indicates the presence of the HT during this season with a positive peak in 50-hPa geopotential height anomaly over southern Australia and a negative peak northwest of the Ross Sea. In the troposphere and the lower stratosphere, the SAM has a regional peak to the east of the HT (see Figs. S3, S6, and S9 in the supplemental material). However, the stratosphere–troposphere coupling suggests that both the SAM and the HT are triggered by a stratospheric signal (Thompson et al. 2005), perhaps similar to the northern annular mode (NAM) (Baldwin and Dunkerton 1999; Baldwin et al. 2003).

4. Impacts on regional climate

The monthly-mean surface temperature patterns over Australia generally follow a north–south gradient, whereas mean precipitation is strongest around the northern and eastern coastal regions with pronounced wet seasons during DJF and MAM (Bureau of Meteorology 2013). Composites of MERRA surface temperature anomalies (Fig. 6) are consistent with the findings in SLP: increased SLP leads to positive (negative) temperature advection and thus higher (lower) surface temperatures to the west (east) due to the counterclockwise rotation around the anomalous high pressure during the whole year. Pezza et al. (2012, their Figs. 8 and 12) have shown how anticyclone synoptic tracks over the Tasman Sea induce heat waves across southern Australia, and the quasi-stationary blocking high system over the Tasman Sea occurs when the baroclinic wave train propagates from the south Indian to the Pacific Ocean (Boschat et al. 2014). However, there is a negative (positive) temperature anomaly around New Zealand during DJF (JJA), partly due to the zonal shift of the southern center. The cold anomaly around Wilkes Land and Adélie Land in

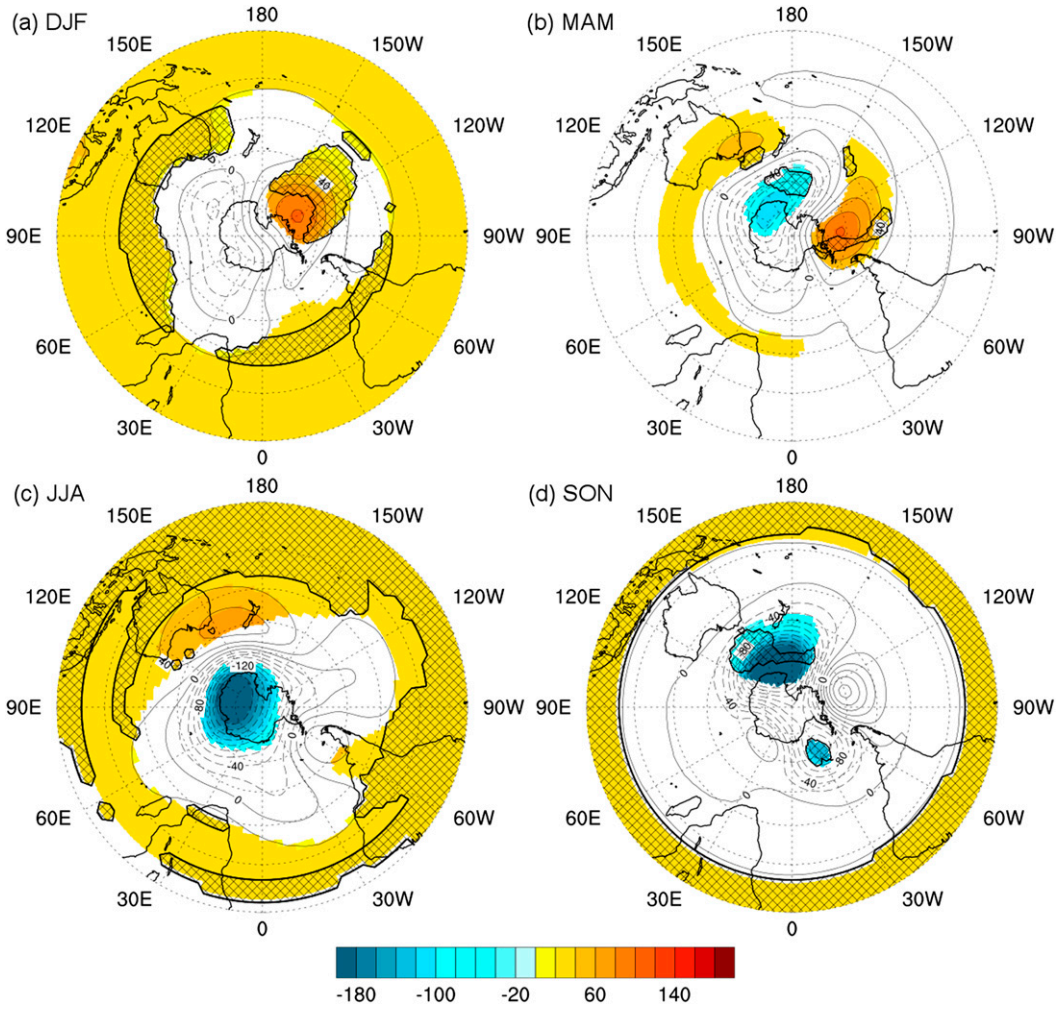

FIG. 5. As in Fig. 3, but for 50-hPa geopotential height (m).

Antarctica during MAM and JJA is mostly related to SAM. A cold anomaly off the coast of Antarctica independent of SAM occurs during SON when the southern SLP signal is also largely independent of SAM.

Figure 7 shows the influence of the HT on the Global Precipitation Climatology Project (GPCP) rainfall anomalies (Adler et al. 2003). Precipitation over southeastern Australia decreases during the positive phase of the HT in all seasons apart from MAM. The largest extent during JJA also covers southwestern Australia, where JJA is the rainy season (Simmonds and Hope 1997). This reduced precipitation is in agreement with the IOD and ENSO pattern during JJA and SON (see Figs. S13 and S14 in the supplemental material). However, although Simmonds and Rocha (1991) found the IOD influence to be stronger during its negative phase, the present study detects a noteworthy difference between the spatial influences of each phase of the HT only during DJF, when IOD is inactive, but the ENSO influence is strongest (not shown). This finding is in line with Cai and van Rensch (2013, their Fig. 5). Significant increases in precipitation occur over parts of central Australia during the DJF and MAM monsoon seasons due to increased SLP over New Zealand, related downdrafts, and southward moisture advection from the equator to northeastern Australia, in conjunction with El Niño conditions over the tropical central Pacific (see Fig. S13). It should be noted that the significant increase in MAM occurs because March is part of the wet season with strong variability in precipitation, whereas April marks the transition into the dry season. Strong changes in March are thus joined with small but significant changes in May and insignificant changes in April (not shown). A decrease (increase) in SLP is also related to positive (negative) rainfall anomalies independent of ENSO and SAM over the Southern Ocean (northern New Zealand) throughout the year.

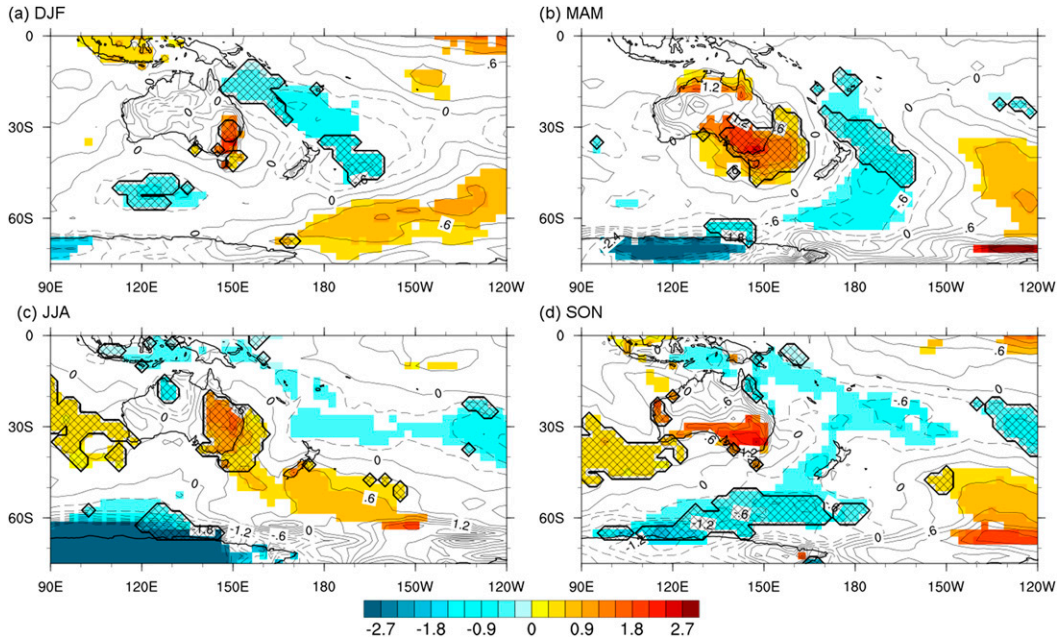

FIG. 6. As in Fig. 3, but for surface temperature (K).

Annual composites of zonal cross sections of the three-dimensional wind anomalies averaged between 150°E and the date line (Figs. 8a,b) reveal westerly and upward (easterly and downward) wind anomalies around the equator and between 35° and 60°S during the positive (negative) phase of the HT, and opposite behavior between 10° and 35°S. The zonal wind response is consistent with the ENSO influence in L'Heureux and Thompson (2006, their Figs. 2 and 8). However, the centers of the HT show about 3 times larger amplitudes in our study than in L'Heureux and Thompson (2006), who average over a 3 times wider zone of the cold

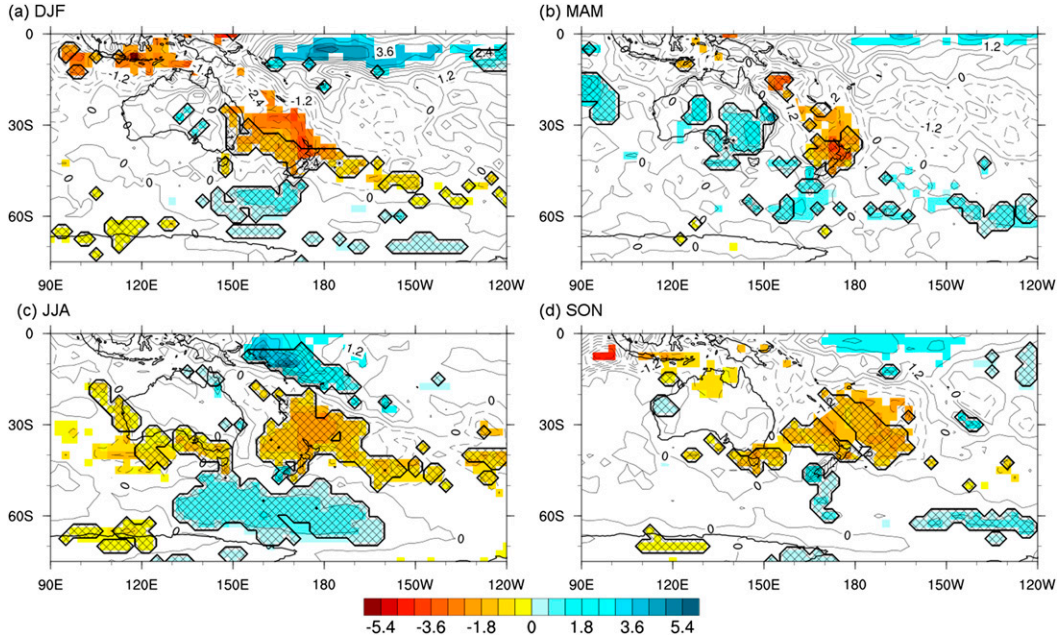

FIG. 7. As in Fig. 3, but for precipitation (mm day^{-1}). Note: shading for precipitation is reversed (blue represents positive rainfall anomalies).

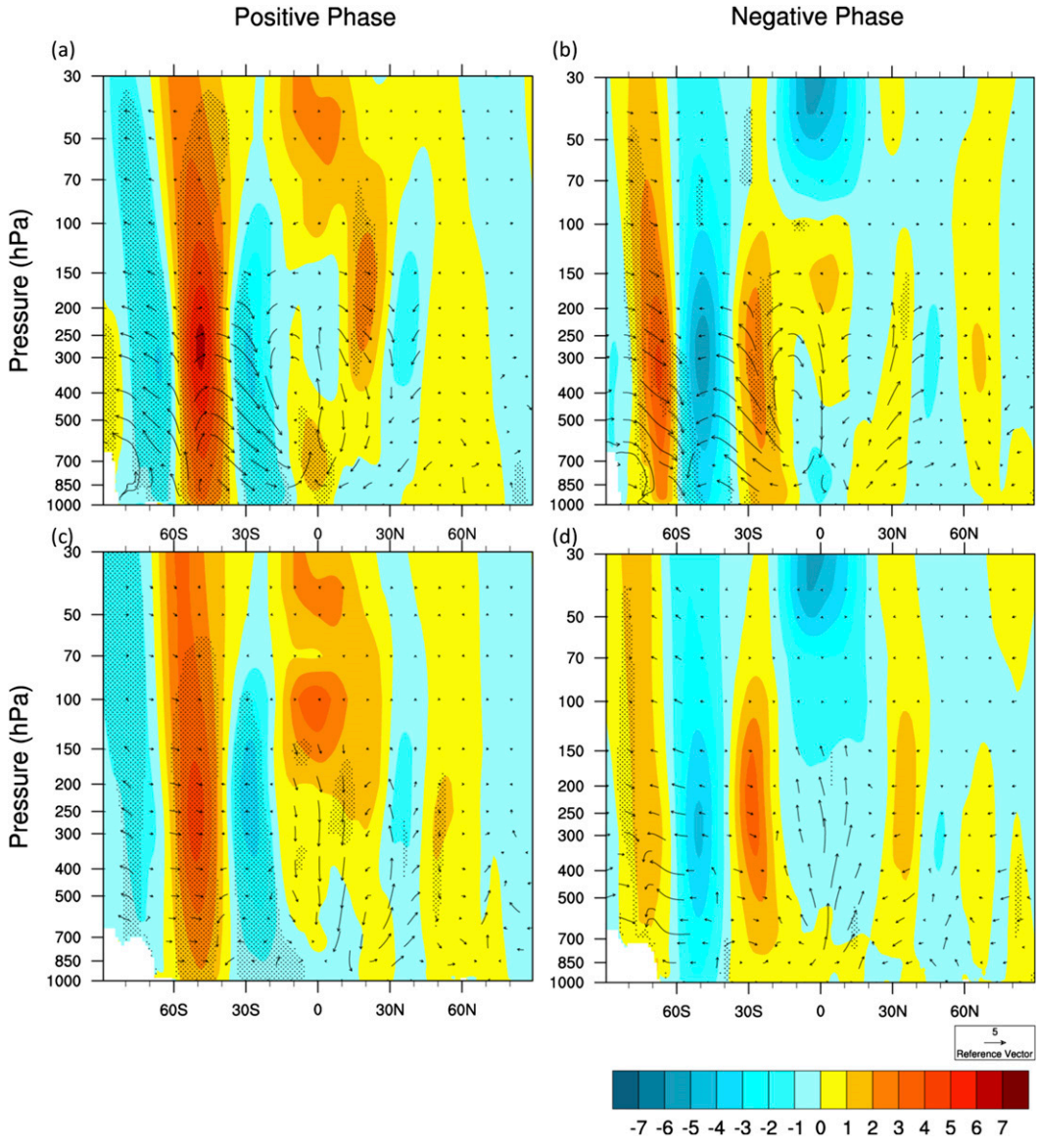

FIG. 8. Anomalies of zonal wind (shaded; m s^{-1}) and meridional circulation (vectors; m s^{-1} and hPa day^{-1}) for the (a) positive and (b) negative phase of the HT averaged over longitudes around the Tasman Sea and New Zealand (150°E–180°). (c),(d) As in (a),(b), but over longitudes around Australia (110°–150°E). Stippling indicates statistically significant differences at 95% between both phases in the zonal wind component in (a) and (c) and in the vertical wind component in (b) and (d) using a *t* test.

tongue index between 180° and 90°W to describe ENSO variations and thus smooth out the smaller-scale peaks in Rossby wave activity. The meridional circulation consists of largely southerly (northerly) winds between 50°S and the equator during the positive (negative) phase. Respective vertical winds are largely downward (upward) over the Tasman Sea and New Zealand, and upward (downward) over the Southern Ocean. The vertical wind pattern is consistent with the rainfall patterns in Fig. 7. In addition to the statistically significant updrafts around 60°S and downdrafts around 20°S during the positive phase and opposite behavior during the negative phase, a significant vertical wind signal is found in the upper troposphere around 30°–40°N over the southern center of the west Pacific (WP) pattern, which reflects the teleconnection between Kamchatka (50°N) and the tropical western Pacific around 20°–30°N (Wallace and Gutzler 1981; Barnston and Livezey 1987; Linkin and Nigam 2008). This is related to the extratropical ENSO influence found by Robinson (2002) and

L'Heureux and Thompson (2006). This zonally averaged thermal response is a product of the thermally indirect secondary circulation driven by eddies (Robinson 2002). Although small in size, this pattern suggests that the forcings for WP and the HT might be related. L'Heureux and Thompson (2006) concluded that the signature of ENSO in the extratropical Southern Hemisphere zonal-mean circulation is driven by variations in the eddy momentum flux at midlatitudes, and poleward propagating Rossby waves show a tendency for a cyclonic center over the Tasman Sea (Cai and van Rensch 2013).

Figures 8c and 8d are similar to the composites shown in Figs. 8a and 8b but instead are averaged between the longitudes around Australia (110° and 150°E). Despite almost identical zonal wind anomalies, the meridional circulation anomaly is reversed between 50°S and 30°N around these longitudes, with divergence around 50°S being replaced by convergence, and anomalous equatorward flow around 30°S being replaced by poleward flow. Anomalous updrafts and downdrafts around the equator and 30°N, respectively, are replaced by opposite vertical flow. This indicates the opposite phase of waves related to the ACC and a potential connection to the Northern Hemisphere subtropics (L'Heureux and Thompson 2006). The westward tilt with height as shown in Figs. 3 and 4 is especially visible during the negative phase, when maximum winds occur around 250 hPa over Australia (Fig. 8d) and around 300 hPa over the Tasman Sea (Fig. 8b).

The Eliassen–Palm (EP) flux and its divergence describe wave propagation based on meridional eddy momentum and heat fluxes, and EP flux divergence indicates westerly forcing (Edmon et al. 1980; Andrews 1987). The EP flux [Edmon et al. 1980, their Eqs. (3.1a) and (3.1b)] and its divergence are calculated from 3-hourly MERRA data and are averaged over 150°E–180° for the positive and negative phases during all four seasons (Fig. 9). Quasigeostrophic scaling (Andrews et al. 1987) has been adopted in Fig. 9 to assist in diagnosing planetary wave activity. However, the scaling in Edmon et al. [1980, their Eq. (3.13)] has been modified according to National Oceanic and Atmospheric Administration (NOAA)/Earth System Research Laboratory (ESRL) (2014):

$$\{\tilde{F}_\phi, \tilde{F}_p\} = \cos\phi \left\{ \frac{F_\phi}{r_0 \pi}, \frac{F_p}{10^5} \right\} \sqrt{\frac{10^5}{p}}, \qquad (2)$$

where r_0 is the radius of Earth, ϕ is the latitude, p is the pressure coordinate (in pascals), and F_ϕ and F_p are the meridional and vertical components of the EP flux, respectively. EP flux divergence has not been scaled.

In the lower troposphere, the poleward eddy momentum flux between 60° and 30°S is increased during the positive phase, consistent with the stronger meridional pressure and temperature gradients (Figs. 3 and 6). The eddy heat flux is stronger between 60° and 45°S and weaker between 45° and 30°S, resulting in positive northward temperature advection (Fig. 6). Wave activity is strongest around 60°S at 400 hPa, and equatorward of 30°S at 300 hPa. This wave energy is taken from the mean westerlies, as indicated by easterly anomalies (Fig. 8a). The two negative peaks in EP flux divergence around these regions show the wave dissipation.

Differences in EP flux between the positive and negative phase are strongest in the MAM and JJA seasons, when the hybrid index is mostly associated with SAM (Table 1). EP flux differences at lower latitudes are more pronounced during SON and DJF, when the HTI is partly correlated to the tropical signals from IOD and ENSO (Cai et al. 2011c). These tropical signals excite extratropical waves around 30°S in the negative phase during DJF (seen by EP flux divergence in Fig. 9b). Also, EP flux convergence is reduced during SON (Fig. 9h).

During the negative phase, wave activity is strongest between 60° and 40°S, with a distinct EP flux divergence over the Tasman Sea equatorward of 30°S around 200 hPa in JJA, which accelerates the mean westerlies (Fig. 8b). In SON and DJF, reduced EP flux convergence around 200 hPa also maintains stronger westerlies equatorward of 30°S during the negative phase compared to the positive phase. The eddy heat flux during JJA is even equatorward in this region, following the meridional circulation anomaly (Fig. 8b). During the positive phase, the average vertical EP flux component between 60° and 45°S in the lower troposphere below 500 hPa is 130% stronger than during the negative phase and 30%–50% stronger between SON and MAM. In the stratosphere, it is still more than 100% stronger in JJA and 25% stronger in SON, but no discernible increase occurs in DJF and MAM. Thus, the positive phase may be linked to sudden stratospheric warming events in the Southern Hemisphere, which primarily occur between August and November (Thompson et al. 2005).

An interaction with the Northern Hemisphere can be assessed by linking eddy momentum fluxes between the hemispheres (L'Heureux and Thompson 2006): the tropospheric eddy momentum flux is stronger in both hemispheres during the positive phase for most seasons, especially during JJA and SON, and the wintertime stratospheric eddy momentum flux is stronger in both hemispheres during the negative phase. The latter is related to weaker meridional pressure gradients and

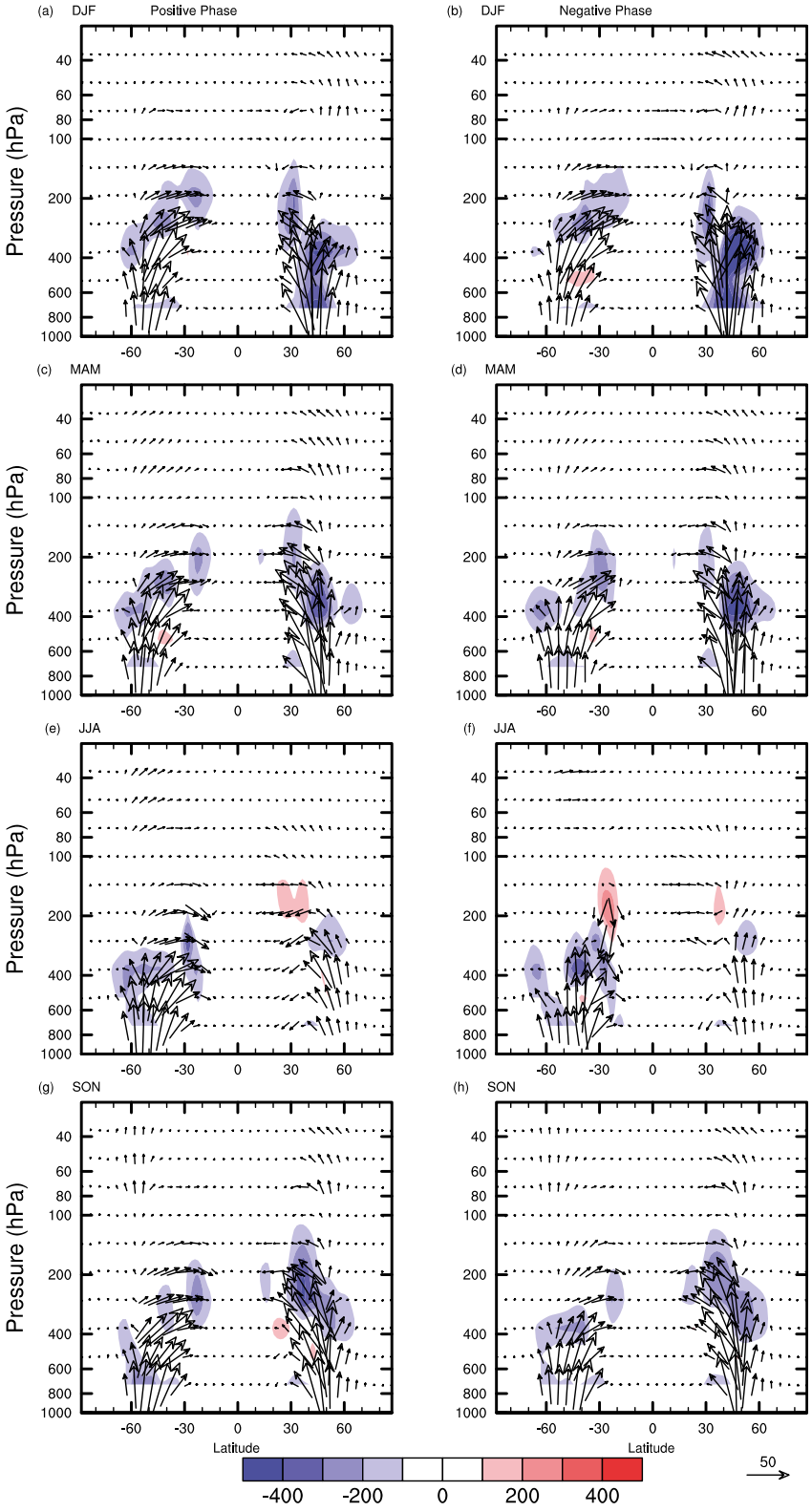

FIG. 9. EP flux (vectors; $m^2 s^{-2}$) and EP flux divergence (shaded; $m^2 s^{-2}$) for (left) positive and (right) negative HT phases for (a),(b) DJF, (c),(d) MAM, (e),(f) JJA, and (g),(h) SON. Quasigeostrophic scaling has been applied and the EP flux above 100 hPa is magnified by a factor of 5.

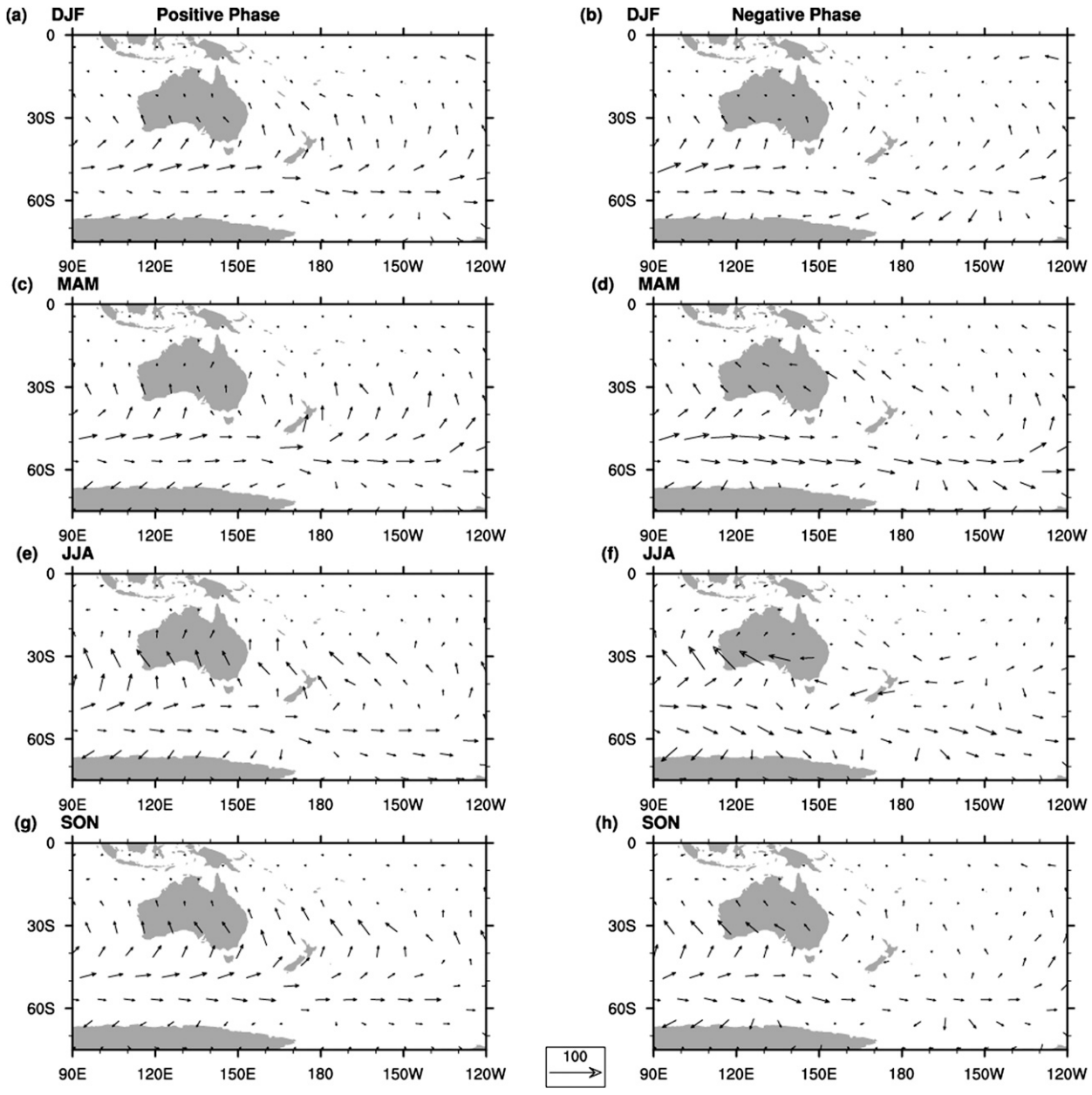

FIG. 10. The 300-hPa $\mathbf{E}_u$ vectors ($m^2 s^{-2}$) after Hoskins et al. (1983) and Trenberth (1991) for (left) positive and (right) negative HT phases for (a),(b) DJF, (c),(d) MAM, (e),(f) JJA, and (g),(h) SON.

thus reduced zonal mean flow despite the strong meridional temperature gradient during winter.

The regional propagation of eddies and their feedback to the mean flow are related to the eddy vorticity flux. It can be approximated by the regional $\mathbf{E}_u$ vector (Hoskins et al. 1983). The meridional component $-\overline{u'v'}$ is defined as the negative of the eddy momentum flux, and the zonal component $1/2(\overline{v'^2} - \overline{u'^2})$ is half the monthly average of the difference between squared meridional and zonal 3-hourly anomalies. The $\mathbf{E}_u$ divergence indicates westerly forcing (Trenberth 1991; Fogt et al. 2011). Figure 10 shows 300-hPa $\mathbf{E}_u$ vectors for the four seasons.

The positive phase shows a northward component over Australia and New Zealand, and stronger eastward propagation around 50°S south of the Tasman Sea. This stronger eastward propagation is related to the strong polar jet (Figs. 8a,c) and high-pass filtered eddies (Hoskins et al. 1983, their Fig. 11a) from short-term jet streaks that can form when jet streams merge (Reiter and Whitney 1969; Cunningham and Keyser 2000). In

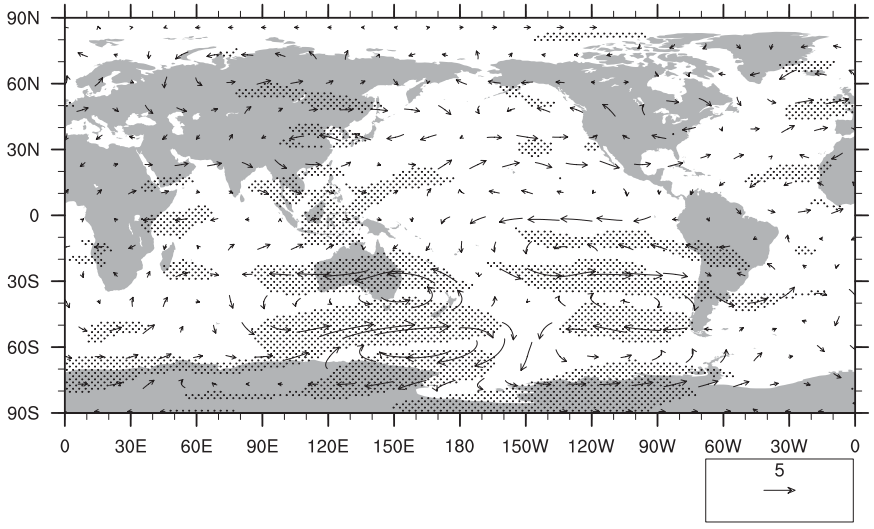

FIG. 11. The 300-hPa wind vector anomalies ($m\,s^{-1}$) for positive minus negative HT phases. Stippling indicates statistically significant differences in the u wind at the 95% confidence level using a t test.

this case, the $\mathbf{E}_u$ convergence north of 30°S decelerates the subtropical jet.

The negative phase is dominated by westward eddy propagation around 30°S, especially over Australia, at the southern limit of the subtropical jet stream (Figs. 8b,d) related to low-pass filtered eddies (Hoskins et al. 1983, their Fig. 11b) from the mean flow. West of Australia, the warmer SST anomalies associated with the negative IOD signal may lead to the negative zonal eddy momentum flux especially in JJA and SON, when the IOD is active. In JJA, the reduced equatorward meridional component over the Tasman Sea during the negative phase highlights the equatorward eddy momentum flux in line with the equatorward eddy heat flux from the negative IOD phase. However, in addition to the seasonal IOD influence, the meridional $\mathbf{E}_u$ component is less equatorward in all seasons during the negative phase. Furthermore, the polar jet is shifted poleward to 60°S, as indicated by stronger eastward eddy propagation in all seasons.

The annual 300-hPa wind field anomalies (Fig. 11) indicate statistically significant changes in the zonal component in line with the poleward Rossby wave propagation over the Tasman Sea (Cai and van Rensch 2013). As previously shown in Fig. 8, this wave propagation points out that the positive phase is related to a reduced subtropical jet, possibly even a merging with the polar jet, whereas the subtropical jet is strengthened in the negative phase. A wider gap between both jets indicates a different type of blocking usually found around 45°S (e.g., Pook and Gibson 1999; Pook et al. 2013). Figure 11 also shows the PSA pattern in relation to ENSO. Other teleconnections in the Northern Hemisphere such as North Atlantic Oscillation (NAO) and the Pacific–North American (PNA) pattern indicate statistically significant changes in the zonal wind field, but possible physical connections would require further investigation of global SST patterns, which is beyond the scope of this study.

5. Long-term variability of the hybrid teleconnection and precipitation extremes

The normalized HTI has also been calculated for 1901–2011 HadSLP2 data (Fig. 12). It shows that the 1979–2011 subsample used in this study captures most of the variability and long-term trend of the longer 111-yr time series. However, it should be noted that the extreme events in Fig. 12 are not necessarily identical to the composite members previously found in the 1979–2011 interval because the time series are detrended over different intervals. An extended Australian drought termed the "Millennium Drought" or "Big Dry" started in the early 1990s (Leblanc et al. 2009; Kiem and Verdon-Kidd 2010) and ended with heavy flooding in the summer of 2010/11 (Blunden et al. 2011; Cai and van Rensch 2012; Wilby and Keenan 2012). In the 1979–2011 period, strong positive hybrid events (exceeding twice the standard deviation) occurred in August 1982 and more frequently during the Millennium Drought with 14 events between June 1993 and November 2010. Ten of these events happened during the winter and spring seasons. The importance of the subtropical ridge, especially during JJA, for declining rainfall was noted by

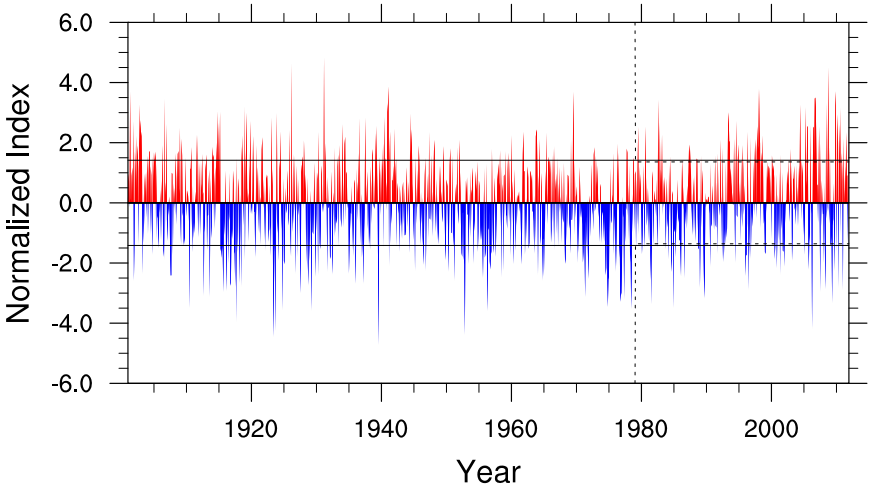

FIG. 12. Hybrid SLP teleconnection for 1901–2011 (northern minus southern center, both detrended and normalized by their standard deviation). Standard deviation of index for 1901–2011 (horizontal solid) and 1979–2011 (vertical dashed), and January 1979 marker (horizontal dashed).

Timbal and Drosdowsky (2013). In addition to the strength of the subtropical ridge, a southward shift of the mean location in MAM has led to a decrease in MAM rainfall since around the 1950s (Whan et al. 2014). Eleven strongly negative events occurred between 1979 and 2011. They were more evenly spread out throughout the whole period, and only four occurred during the winter and spring seasons.

Drought events during strong positive phases seem to contradict Fig. 7 and the findings of Klingaman et al. (2013). However, it is important to note that strong positive phases are related to large expansions of the high-pressure system over the Tasman Sea. These large high-pressure systems can cover most of Australia and New Zealand (Fig. 13a) and can lead to a significant decrease in rainfall mainly over the southern coastal fringes of Australia and over northern New Zealand (Fig. 13b). Precipitation over parts of central Australia is significantly increased for index amplitudes of up to 1.4 standard deviations and decreases for amplitudes above 1.8 for the 1979–2011 period (not shown). The overall precipitation response remains weak due to the transient nature of the atmospheric waves related to the HT. However, an increase in surface temperature (see Fig. 6) increases evapotranspiration, which can reduce soil moisture and surface water storages (Leblanc et al. 2009) and thus can contribute to long-term droughts.

Large amplitudes in the index time series were also found during the 1920s–1940s period, when another long-term drought influenced Australia's climate: the "World War II drought" from 1937 to 1945 (Verdon-Kidd and Kiem 2009). In this case, 6 out of 10 strong positive events occurred during the drought period, with 4 of these in JJA and SON. In the two decades before the drought, there were no positive events in JJA and SON as well as seven negative events, mostly in JJA and SON. Only one negative event occurred during this drought.

During the 1940s as well as during the 1990s, the Pacific decadal oscillation (PDO) was mostly in the positive phase (Mantua and Hare 2002), and the Atlantic multidecadal oscillation (AMO; Delworth and Mann 2000) went from the negative to the positive phase. For 1901–2011, 5-yr means of the detrended PDO index and the HTI are lag-correlated at 0.60 when the PDO leads by 5 yr. Five-year means of the detrended AMO index and the HTI are correlated at 0.38 and lag-correlated at −0.59, when the AMO leads the HT by 25 yr. However, at this point we can only speculate that the PDO and/or AMO are linked to this teleconnection via the general circulation and large-scale oscillations such as ENSO. Previously, AMO signals have been detected in North and South American rainfall (Teegavarapu et al. 2013; Kayano and Capistrano 2014), and Zanchettin et al. (2014, their Fig. 3) have shown opposite impacts of North Atlantic SSTs on the Tasman Sea versus the Southern Ocean region to the south in model simulations.

The increase in occurrence of both strong positive and negative events (at least twice the standard deviation) during the beginning of the twenty-first century can thus either be attributed to multidecadal variability, as indicated by similar events during the 1940s, or anthropogenic climate change related to stronger pressure gradients between polar and midlatitudinal regions (e.g., Gillett and Stott 2009). To show the long-term

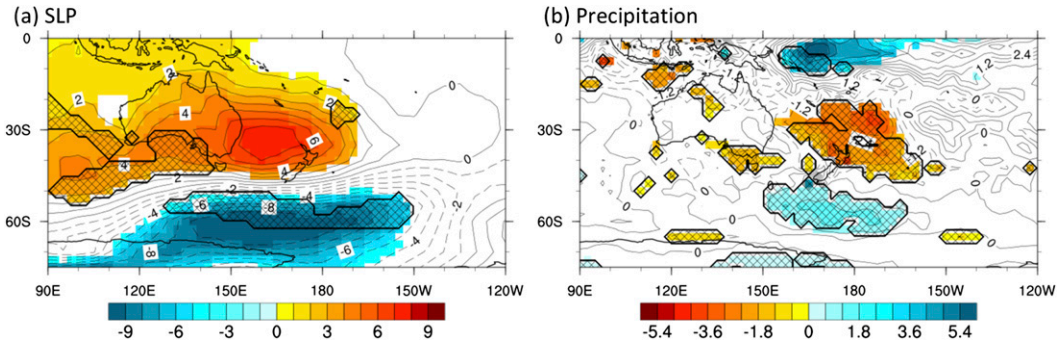

FIG. 13. Annual (a) HadSLP2 (hPa) and (b) precipitation (mm day^{-1}) composites for thresholds of twice the standard deviation. Shading indicates 95% significance level. Hatching represents areas that are significant for the hybrid teleconnection, but not for SAM, ENSO, or IOD.

variability of the HT, correlations between northern and southern centers during 31-yr windows for HadSLP2 anomalies are calculated (Fig. 14). As shown in Tables 1 and 2, the strongest correlations are found during JJA, when the stratospheric signal is strong and related to SAM (see Fig. S9 in the supplemental material). Correlations are also strong during SON. The IOD signal is also strongest during these two seasons. Correlations are weakest and mostly not significant during DJF (see also Tables 1 and 2) due to the interplay between SAM and ENSO. Five-year means of the AMO lead the strength of the HT during all months by 5 yr at a lag correlation of 0.53, which is based on similar values of 0.56 and 0.59 during JJA and SON, while the lag correlation during MAM is negative at −0.80. There is no statistically significant relationship between the PDO and the strength of the 31-yr HT correlation. Although this statistical analysis suggests a relation between global SST patterns and the long-term variations of the HT, the physical mechanisms guiding these regional impacts and the influence of stochastic processes need to be further addressed, for example by forcing an atmospheric general circulation model with SSTs from different AMO and PDO phases.

Dean and Stott (2009) described a zonal teleconnection in annual mean SLP between Tasmania and the Chatham Islands east of New Zealand. Their M1 index shows peak periods in SLP that are similar to our results with positive anomalies during the 1900s, 1940s, and 1990s, and negative anomalies during the 1920s, 1950s, and 1970s. However, the present study allows for a more quantitative localization of the centers of action, and buoys placed around these centers could provide useful information for regional weather forecasts and seasonal climate projections.

6. Discussion and conclusions

The HT combines the phases of ENSO and SAM over the Tasman Sea and the Southern Ocean where the two teleconnections interact at times. An additional interaction with the IOD is strongly related to the ENSO signal (see Figs. S1 and S2 in the supplemental material). The centers of the HT have been detected with a shared reciprocal nearest neighbor (SRNN) approach (Kawale et al. 2013), which does not require a priori data selection or imposing an orthogonality constraint as in EOF analysis. The newly identified HT contains a residual that is statistically not accounted for by ENSO, IOD, or SAM. Thus, it can be treated as an independent teleconnection. The HT can provide a climate index relevant for part of Australia and New Zealand, especially over the densely populated regions of southeastern Australia and northern New Zealand. Meandering jet streams can form a jet streak with a high-pressure system to its north and a low pressure system to its south. These form the centers of the HT. Composites of the meridional circulation and the global 300-hPa wind field

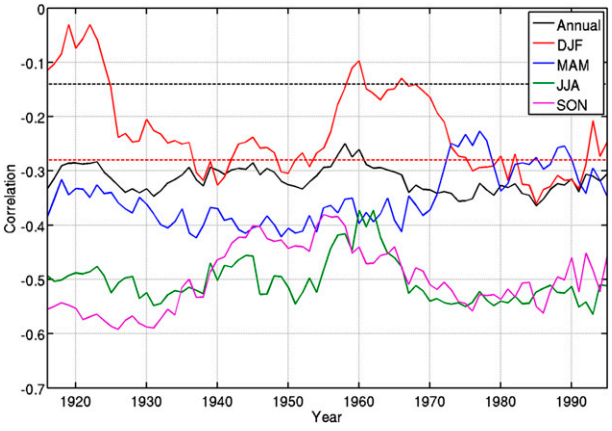

FIG. 14. Strength of the HT for all months and each season during running 31-yr intervals (1901–2011). The x axis shows the center of each interval (1916–95). The dashed black and red lines indicate the 95% confidence interval for annual and seasonal correlations, respectively.

suggest that midlatitudinal teleconnections over the Southern and Northern Hemispheres are subject to similar tropical forcings, such as ENSO.

L'Heureux and Thompson (2006) attributed the influence of ENSO over this region to horizontal eddy momentum fluxes, which is confirmed in this study. Furthermore, composites based on the HT are related to meridional heat and momentum fluxes in the stratosphere, and similar patterns over the Northern Hemisphere suggest interaction with the WP pattern. Additionally, Liess and Geller (2012) found an influence of the stratospheric quasi-biennial oscillation (QBO) on tropical and subtropical deep convection through modifications of the Hadley circulation, which indicates correlations between Northern and Southern Hemispheric flow, especially related to the deep convection over the western Pacific warm pool. Other indices such as the M1 index from Dean and Stott (2009) emphasize the relevance of wave trains around the region of interest for climate over southeastern Australia and New Zealand.

Kiem and Verdon-Kidd (2010, their Table 4) highlighted the influence of El Niño and the positive SAM phase for Australian droughts, whereby the positive SAM phase is related to droughts only during MAM and JJA (Hendon et al. 2007). Ummenhofer et al. (2009) suggested the importance of the IOD for Australian droughts. While the strongest drought signal is related to ENSO and the IOD, the SAM was mostly in the positive phase during DJF and MAM between the early 1990s and 2010, especially during the 1999, 2000, and 2008 La Niña events. The SAM was negative during the beginning of 2001 and coincided with the La Niña pattern, thus coinciding with above average rainfall during that year. However, SAM is an annular mode that consists mostly of transient eddies (Matthewman and Magnusdottir 2012), and its quasi-stationary pattern is shifted eastward compared to the interactions over the Tasman Sea (see Fig. S3 in the supplemental material). Thus, SAM-related warming occurs mostly over New Zealand while Australia exhibits cooling in all seasons (see Fig. S12). The significant influence of the monthly SAM on Australian rainfall (see Fig. S15) is similar to daily composites shown in Hendon et al. (2007, their Fig. 3). Using seasonal SLP-based indices such as AOI and AOIR, Meneghini et al. (2007) are also able to extract the SAM signal relevant for Australian rainfall. However, the HT related to SAM in JJA and ENSO in DJF provides an additional predictor of drought periods, especially when the associated index exceeds twice the standard deviation.

The HT can also be detected by relating the Southern Hemisphere winter modes to SAM and the Pacific–South American pattern (Matthewman and Magnusdottir 2012, their Fig. 5c). These interactions between teleconnections provide the potential for relationships between other large-scale teleconnections: the axisymmetric modes of the SAM and the northern annular mode (NAM) are disturbed by differential heating, partly due to land–sea contrasts. It is suggested that NAM is not only closely related to the NAO (Wallace 2000; Feldstein and Franzke 2006), but is also related to the PNA (Thompson and Wallace 2001), although distinctly different patterns emerge over the Pacific because of interactions with regional ocean currents (Taguchi et al. 2012).

The western North Pacific portion of the NAM is dominated by the WP pattern. Thus, the western South Pacific portion of the SAM, which is described here, can connect NAM and SAM around the western Pacific warm pool (see Fig. 11) given the strong forcing from tropical deep convection and the resulting meridional transient eddy momentum flux (L'Heureux and Thompson 2006).

Although multiple studies have identified ENSO, IOD, and SAM as useful predictors of seasonal Australian rainfall (Schepen et al. 2012a,b), the HT is suggested to be an additional predictor for Australian and New Zealand climate variability. Not only the baroclinic wave trains but also the multidecadal SLP trends show distinct differences between different seasons. Pressure trends over the last few decades exhibit a strong annular structure in summer, whereas the SAM trend is barely significant and limited to the Pacific and Indian Ocean in fall (Simmonds 2014). Apart from the positive SAM trend, also positive HT events in recent decades coincide with reduced surface temperatures over the Antarctic coastline (Fig. 7) and thus an increase in sea ice extent, especially in MAM and JJA (Simmonds 2014).

The relationship between the positive HTI and long-term droughts can primarily be explained by large high-pressure anomalies when the positive index phase is above twice the standard deviation, whereas smaller phase changes mainly contribute toward redistributing the regional rainfall. Further analysis of these teleconnection interactions on the regional climate may aid in improving predictability of the seasonal climate.

Acknowledgments. HadSLP2 and AMO data were provided by the Met Office (UKMO). SAM and ENSO indices were obtained from the Climate Prediction Center (CPC), and the DMI was retrieved from JAMSTEC. The MERRA reanalysis was received from NASA's Modeling and Assimilation Data and Information Services Center, and GPCP precipitation and PDO index data were made available by NOAA's Earth System Research Laboratory. The authors are grateful for the

comments of three anonymous reviewers that have greatly improved this manuscript. This research was supported by the U.S. National Science Foundation under Grant IIS-1029711. Access to computing facilities was made available by the Minnesota Supercomputing Institute. This study benefited from the work of undergraduate researchers D. Ormsby and T. Rehberger.

REFERENCES

Adler, R. F., and Coauthors, 2003: The version-2 Global Precipitation Climatology Project (GPCP) monthly precipitation analysis (1979–present). *J. Hydrometeor.,* **4,** 1147–1167, doi:10.1175/1525-7541(2003)004<1147:TVGPCP>2.0.CO;2.

Allan, R., and T. Ansell, 2006: A new globally complete monthly historical gridded mean sea level pressure dataset (HadSLP2): 1850–2004. *J. Climate,* **19,** 5816–5842, doi:10.1175/JCLI3937.1.

Andrews, D. G., 1987: On the interpretation of the Eliassen–Palm flux divergence. *Quart. J. Roy. Meteor. Soc.,* **113,** 323–338, doi:10.1002/qj.49711347518.

——, F. W. Taylor, and M. E. McIntyre, 1987: The influence of atmospheric waves on the general circulation of the middle atmosphere. *Philos. Trans. Roy. Soc.,* **323A,** 693–705, doi:10.1098/rsta.1987.0115.

Baldwin, M. P., and T. J. Dunkerton, 1999: Propagation of the Arctic Oscillation from the stratosphere to the troposphere. *J. Geophys. Res.,* **104,** 30 937–30 946, doi:10.1029/1999JD900445.

——, D. W. J. Thompson, E. F. Shuckburgh, W. A. Norton, and N. P. Gillett, 2003: Weather from the stratosphere? *Science,* **301,** 317–319, doi:10.1126/science.1085688.

Barnston, A. G., and R. E. Livezey, 1987: Classification, seasonality and persistence of low-frequency atmospheric circulation patterns. *Mon. Wea. Rev.,* **115,** 1083–1126, doi:10.1175/1520-0493(1987)115<1083:CSAPOL>2.0.CO;2.

Blunden, J., D. S. Arndt, and M. O. Baringer, 2011: State of the climate in 2010. *Bull. Amer. Meteor. Soc.,* **92,** S1–S236, doi:10.1175/1520-0477-92.6.S1.

Boschat, G., A. Pezza, I. Simmonds, S. Perkins, T. Cowan, and A. Purich, 2014: Large scale and sub-regional connections in the lead up to summer heat wave and extreme rainfall events in eastern Australia. *Climate Dyn.,* doi:10.1007/s00382-014-2214-5, in press.

Bureau of Meteorology, cited 2013: Climate and past weather. [Available online at http://www.bom.gov.au/climate.]

Cai, W., and P. van Rensch, 2012: The 2011 southeast Queensland extreme summer rainfall: A confirmation of a negative Pacific decadal oscillation phase? *Geophys. Res. Lett.,* **39,** L08702, doi:10.1029/2011GL050820.

——, and ——, 2013: Austral summer teleconnections of Indo-Pacific variability: Their nonlinearity and impacts on Australian climate. *J. Climate,* **26,** 2796–2810, doi:10.1175/JCLI-D-12-00458.1.

——, A. Sullivan, and T. Cowan, 2011a: Interactions of ENSO, the IOD, and the SAM in CMIP3 models. *J. Climate,* **24,** 1688–1704, doi:10.1175/2010JCLI3744.1.

——, P. van Rensch, S. Borlace, and T. Cowan, 2011b: Does the southern annular mode contribute to the persistence of the multidecade-long drought over southwest Western Australia? *Geophys. Res. Lett.,* **38,** L14712, doi:10.1029/2011GL047943.

——, ——, T. Cowan, and H. H. Hendon, 2011c: Teleconnection pathways of ENSO and the IOD and the mechanisms for impacts on Australian rainfall. *J. Climate,* **24,** 3910–3923, doi:10.1175/2011JCLI4129.1.

——, X.-T. Zheng, E. Weller, M. Collins, T. Cowan, M. Lengaigne, W. Yu, and T. Yamagata, 2013: Projected response of the Indian Ocean dipole to greenhouse warming. *Nat. Geosci.,* **6,** 999–1007, doi:10.1038/ngeo2009.

Cowan, T., P. van Rensch, A. Purich, and W. Cai, 2013: The association of tropical and extratropical climate modes to atmospheric blocking across southeastern Australia. *J. Climate,* **26,** 7555–7569, doi:10.1175/JCLI-D-12-00781.1.

Cunningham, P., and D. Keyser, 2000: Analytical and numerical modelling of jet streaks: Barotropic dynamics. *Quart. J. Roy. Meteor. Soc.,* **126,** 3187–3217, doi:10.1002/qj.49712657010.

Dean, S. M., and P. A. Stott, 2009: The effect of local circulation variability on the detection and attribution of New Zealand temperature trends. *J. Climate,* **22,** 6217–6229, doi:10.1175/2009JCLI2715.1.

Delworth, T. L., and M. E. Mann, 2000: Observed and simulated multidecadal variability in the Northern Hemisphere. *Climate Dyn.,* **16,** 661–676, doi:10.1007/s003820000075.

Dommenget, D., and M. Latif, 2002: A cautionary note on the interpretation of EOF. *J. Climate,* **15,** 216–225, doi:10.1175/1520-0442(2002)015<0216:ACNOTI>2.0.CO;2.

Edmon, H. J., B. J. Hoskins, and M. E. McIntyre, 1980: Eliassen–Palm cross sections for the troposphere. *J. Atmos. Sci.,* **37,** 2600–2616, doi:10.1175/1520-0469(1980)037<2600:EPCSFT>2.0.CO;2.

Feldstein, S. B., and C. Franzke, 2006: Are the North Atlantic Oscillation and the northern annular mode distinguishable? *J. Atmos. Sci.,* **63,** 2915–2930, doi:10.1175/JAS3798.1.

Fogt, R., D. Bromwich, and K. Hines, 2011: Understanding the SAM influence on the South Pacific ENSO teleconnection. *Climate Dyn.,* **36,** 1555–1576, doi:10.1007/s00382-010-0905-0.

Gillett, N. P., and P. A. Stott, 2009: Attribution of anthropogenic influence on seasonal sea level pressure. *Geophys. Res. Lett.,* **36,** L23709, doi:10.1029/2009gl041269.

Goubanova, K., S. Illig, E. Machu, V. Garçon, and B. Dewitte, 2013: SST subseasonal variability in the central Benguela upwelling system as inferred from satellite observations (1999–2009). *J. Geophys. Res.,* **118,** 4092–4110, doi:10.1002/jgrc.20287.

Hendon, H. H., D. W. J. Thompson, and M. C. Wheeler, 2007: Australian rainfall and surface temperature variations associated with the Southern Hemisphere annular mode. *J. Climate,* **20,** 2452–2467, doi:10.1175/JCLI4134.1.

Hoskins, B. J., I. N. James, and G. H. White, 1983: The shape, propagation and mean-flow interaction of large-scale weather systems. *J. Atmos. Sci.,* **40,** 1595–1612, doi:10.1175/1520-0469(1983)040<1595:TSPAMF>2.0.CO;2.

Hurrell, J. W., 1995: Decadal trends in the North Atlantic Oscillation: Regional temperatures and precipitation. *Science,* **269,** 676–679, doi:10.1126/science.269.5224.676.

Karoly, D. J., 1989: Southern Hemisphere circulation features associated with El Niño–Southern Oscillation events. *J. Climate,* **2,** 1239–1252, doi:10.1175/1520-0442(1989)002<1239:SHCFAW>2.0.CO;2.

Kawale, J., and Coauthors, 2013: A graph-based approach to find teleconnections in climate data. *Stat. Anal. Data Mining,* **6,** 158–179, doi:10.1002/sam.11181.

Kayano, M. T., and V. B. Capistrano, 2014: How the Atlantic multidecadal oscillation (AMO) modifies the ENSO influence on the South American rainfall. *Int. J. Climatol.,* **34,** 162–178, doi:10.1002/joc.3674.

Kiem, A. S., and D. C. Verdon-Kidd, 2010: Towards understanding hydroclimatic change in Victoria, Australia—Preliminary in-

sights into the "Big Dry." *Hydrol. Earth Syst. Sci.,* **14,** 433–445, doi:10.5194/hess-14-433-2010.

Klingaman, N. P., S. J. Woolnough, and J. Syktus, 2013: On the drivers of inter-annual and decadal rainfall variability in Queensland, Australia. *Int. J. Climatol.,* **33,** 2413–2430, doi:10.1002/joc.3593.

Leblanc, M. J., P. Tregoning, G. Ramillien, S. O. Tweed, and A. Fakes, 2009: Basin-scale, integrated observations of the early 21st century multiyear drought in southeast Australia. *Water Resour. Res.,* **45,** W04408, doi:10.1029/2008WR007333.

L'Heureux, M. L., and D. W. J. Thompson, 2006: Observed relationships between the El Niño–Southern Oscillation and the extratropical zonal-mean circulation. *J. Climate,* **19,** 276–287, doi:10.1175/JCLI3617.1.

Liess, S., and M. A. Geller, 2012: On the relationship between QBO and distribution of tropical deep convection. *J. Geophys. Res.,* **117,** D03108, doi:10.1029/2011JD016317.

Linkin, M. E., and S. Nigam, 2008: The North Pacific oscillation–west Pacific teleconnection pattern: Mature-phase structure and winter impacts. *J. Climate,* **21,** 1979–1997, doi:10.1175/2007JCLI2048.1.

Mantua, N. J., and S. R. Hare, 2002: The Pacific decadal oscillation. *J. Oceanogr.,* **58,** 35–44, doi:10.1023/A:1015820616384.

Marshall, G. J., 2003: Trends in the southern annular mode from observations and reanalyses. *J. Climate,* **16,** 4134–4143, doi:10.1175/1520-0442(2003)016<4134:TITSAM>2.0.CO;2.

Matthewman, N. J., and G. Magnusdottir, 2012: Clarifying ambiguity in intraseasonal Southern Hemisphere climate modes during austral winter. *J. Geophys. Res.,* **117,** D03105, doi:10.1029/2011JD016707.

McBride, J. L., and N. Nicholls, 1983: Seasonal relationships between Australian rainfall and the Southern Oscillation. *Mon. Wea. Rev.,* **111,** 1998–2004, doi:10.1175/1520-0493(1983)111<1998:SRBARA>2.0.CO;2.

McIntosh, P. C., A. J. Ash, and M. S. Smith, 2005: From oceans to farms: The value of a novel statistical climate forecast for agricultural management. *J. Climate,* **18,** 4287–4302, doi:10.1175/JCLI3515.1.

Meneghini, B., I. Simmonds, and I. N. Smith, 2007: Association between Australian rainfall and the southern annular mode. *Int. J. Climatol.,* **27,** 109–121, doi:10.1002/joc.1370.

Mo, K. C., 2000: Relationships between low-frequency variability in the Southern Hemisphere and sea surface temperature anomalies. *J. Climate,* **13,** 3599–3610, doi:10.1175/1520-0442(2000)013<3599:RBLFVI>2.0.CO;2.

Nigam, S., 2003: Teleconnections. *Encyclopedia of Atmospheric Sciences,* J. R. Holton, J. A. Curry, and J. A. Pyle, Eds., Academic Press, 2243–2269.

NOAA/ESRL, cited 2014: EP flux from the NCAR/NCEP reanalysis. [Available online at http://www.esrl.noaa.gov/psd/data/epflux/.]

Nowlin, W. D., and J. M. Klinck, 1986: The physics of the Antarctic Circumpolar Current. *Rev. Geophys.,* **24,** 469–491, doi:10.1029/RG024i003p00469.

Pezza, A., P. van Rensch, and W. Cai, 2012: Severe heat waves in Southern Australia: Synoptic climatology and large scale connections. *Climate Dyn.,* **38,** 209–224, doi:10.1007/s00382-011-1016-2.

Pook, M., and T. Gibson, 1999: Atmospheric blocking and storm tracks during SOP-1 of the FROST Project. *Aust. Meteor. Mag.,* **48,** 51–60.

——, S. Lisson, J. Risbey, C. C. Ummenhofer, P. McIntosh, and M. Rebbeck, 2009: The autumn break for cropping in southeast Australia: Trends, synoptic influences and impacts on wheat yield. *Int. J. Climatol.,* **29,** 2012–2026, doi:10.1002/joc.1833.

——, J. S. Risbey, P. C. McIntosh, C. C. Ummenhofer, A. G. Marshall, and G. A. Meyers, 2013: The seasonal cycle of blocking and associated physical mechanisms in the Australian region and relationship with rainfall. *Mon. Wea. Rev.,* **141,** 4534–4553, doi:10.1175/MWR-D-13-00040.1.

Reiter, E. R., and L. F. Whitney, 1969: Interaction between subtropical and polar-front jet stream. *Mon. Wea. Rev.,* **97,** 432–438, doi:10.1175/1520-0493(1969)097<0432:IBSAPJ>2.3.CO;2.

Rienecker, M. M., and Coauthors, 2011: MERRA: NASA's Modern-Era Retrospective Analysis for Research and Applications. *J. Climate,* **24,** 3624–3648, doi:10.1175/JCLI-D-11-00015.1.

Robinson, W. A., 2002: On the midlatitude thermal response to tropical warmth. *Geophys. Res. Lett.,* **29,** 1190, doi:10.1029/2001GL014158.

Ropelewski, C. F., and M. S. Halpert, 1987: Global and regional scale precipitation patterns associated with the El Niño/Southern Oscillation. *Mon. Wea. Rev.,* **115,** 1606–1626, doi:10.1175/1520-0493(1987)115<1606:GARSPP>2.0.CO;2.

Schepen, A., Q. J. Wang, and D. Robertson, 2012a: Evidence for using lagged climate indices to forecast Australian seasonal rainfall. *J. Climate,* **25,** 1230–1246, doi:10.1175/JCLI-D-11-00156.1.

——, ——, and D. E. Robertson, 2012b: Combining the strengths of statistical and dynamical modeling approaches for forecasting Australian seasonal rainfall. *J. Geophys. Res.,* **117,** D20107, doi:10.1029/2012JD018011.

Simmonds, I., 1990: A modelling study of winter circulation and precipitation anomalies associated with Australian region ocean temperatures. *Aust. Meteor. Mag.,* **38,** 151–162.

——, 2003: Modes of atmospheric variability over the Southern Ocean. *J. Geophys. Res.,* **108,** 8078, doi:10.1029/2000JC000542.

——, 2014: Comparing and contrasting the behaviour of Arctic and Antarctic sea ice over the 35 year period 1979–2013. *Ann. Glaciol.,* doi:10.3189/2015AoG69A909, in press.

——, and A. Rocha, 1991: The association of Australian winter climate with ocean temperatures to the west. *J. Climate,* **4,** 1147–1161, doi:10.1175/1520-0442(1991)004<1147:TAOAWC>2.0.CO;2.

——, and P. Hope, 1997: Persistence characteristics of Australian rainfall anomalies. *Int. J. Climatol.,* **17,** 597–613, doi:10.1002/(SICI)1097-0088(199705)17:6<597::AID-JOC173>3.0.CO;2-V.

——, and J. S. King, 2004: Global and hemispheric climate variations affecting the Southern Ocean. *Antarct. Sci.,* **16,** 401–413, doi:10.1017/S0954102004002226.

Stein, K., A. Timmermann, and N. Schneider, 2011: Phase synchronization of the El Niño–Southern Oscillation with the annual cycle. *Phys. Rev. Lett.,* **107,** 128501, doi:10.1103/PhysRevLett.107.128501.

Steinbach, M., P.-N. Tan, V. Kumar, S. Klooster, and C. Potter, 2003: Discovery of climate indices using clustering. *Proc. Ninth ACM SIGKDD Int. Conf. on Knowledge Discovery and Data Mining,* Washington, DC, ACM, 446–455.

Taguchi, B., H. Nakamura, M. Nonaka, N. Komori, A. Kuwano-Yoshida, K. Takaya, and A. Goto, 2012: Seasonal evolutions of atmospheric response to decadal SST anomalies in the North Pacific subarctic frontal zone: Observations and a coupled model simulation. *J. Climate,* **25,** 111–139, doi:10.1175/JCLI-D-11-00046.1.

Teegavarapu, R. S. V., A. Goly, and J. Obeysekera, 2013: Influences of Atlantic multidecadal oscillation phases on spatial

and temporal variability of regional precipitation extremes. *J. Hydrol.,* **495,** 74–93, doi:10.1016/j.jhydrol.2013.05.003.

Thompson, D. W. J., and J. M. Wallace, 2001: Regional climate impacts of the Northern Hemisphere annular mode. *Science,* **293,** 85–89, doi:10.1126/science.1058958.

——, M. P. Baldwin, and S. Solomon, 2005: Stratosphere–troposphere coupling in the Southern Hemisphere. *J. Atmos. Sci.,* **62,** 708–715, doi:10.1175/JAS-3321.1.

Timbal, B., and W. Drosdowsky, 2013: The relationship between the decline of southeastern Australian rainfall and the strengthening of the subtropical ridge. *Int. J. Climatol.,* **33,** 1021–1034, doi:10.1002/joc.3492.

Trenberth, K. E., 1981: Observed Southern Hemisphere eddy statistics at 500 mb: Frequency and spatial dependence. *J. Atmos. Sci.,* **38,** 2585–2605, doi:10.1175/1520-0469(1981)038<2585:OSHESA>2.0.CO;2.

——, 1991: Storm tracks in the Southern Hemisphere. *J. Atmos. Sci.,* **48,** 2159–2178, doi:10.1175/1520-0469(1991)048<2159:STITSH>2.0.CO;2.

——, and J. M. Caron, 2000: The Southern Oscillation revisited: Sea level pressures, surface temperatures, and precipitation. *J. Climate,* **13,** 4358–4365, doi:10.1175/1520-0442(2000)013<4358:TSORSL>2.0.CO;2.

Tsonis, A. A., K. L. Swanson, and P. J. Roebber, 2006: What do networks have to do with climate? *Bull. Amer. Meteor. Soc.,* **87,** 585–595, doi:10.1175/BAMS-87-5-585.

Ummenhofer, C. C., M. H. England, P. C. McIntosh, G. A. Meyers, M. J. Pook, J. S. Risbey, A. Sen Gupta, and A. S. Taschetto, 2009: What causes southeast Australia's worst droughts? *Geophys. Res. Lett.,* **36,** L04706, doi:10.1029/2008GL036801.

——, P. C. McIntosh, M. J. Pook, and J. S. Risbey, 2013: Impact of surface forcing on Southern Hemisphere atmospheric blocking in the Australia–New Zealand sector. *J. Climate,* **26,** 8476–8494, doi:10.1175/JCLI-D-12-00860.1.

van den Dool, H. M., S. Saha, and Å. Johansson, 2000: Empirical orthogonal teleconnections. *J. Climate,* **13,** 1421–1435, doi:10.1175/1520-0442(2000)013<1421:EOT>2.0.CO;2.

Verdon-Kidd, D. C., and A. S. Kiem, 2009: Nature and causes of protracted droughts in southeast Australia: Comparison between the Federation, WWII, and Big Dry droughts. *Geophys. Res. Lett.,* **36,** L22707, doi:10.1029/2009GL041067.

Walker, G. T., and E. W. Bliss, 1932: World Weather V. *Mem. Roy. Meteor. Soc.,* **4,** 53–84.

Wallace, J. M., 2000: North Atlantic Oscillation/annular mode: Two paradigms—One phenomenon. *Quart. J. Roy. Meteor. Soc.,* **126,** 791–805, doi:10.1002/qj.49712656402.

——, and D. S. Gutzler, 1981: Teleconnections in the geopotential height field during the Northern Hemisphere winter. *Mon. Wea. Rev.,* **109,** 784–812, doi:10.1175/1520-0493(1981)109<0784:TITGHF>2.0.CO;2.

Wang, G., and H. H. Hendon, 2007: Sensitivity of Australian rainfall to inter–El Niño variations. *J. Climate,* **20,** 4211–4226, doi:10.1175/JCLI4228.1.

Whan, K., B. Timbal, and J. Lindesay, 2014: Linear and nonlinear statistical analysis of the impact of sub-tropical ridge intensity and position on south-east Australian rainfall. *Int. J. Climatol.,* **34,** 326–342, doi:10.1002/joc.3689.

Wilby, R. L., and R. Keenan, 2012: Adapting to flood risk under climate change. *Prog. Phys. Geogr.,* **36,** 348–378, doi:10.1177/0309133312438908.

Wright, W., 1994: Seasonal climate summary Southern Hemisphere (autumn 1993)—A second mature ENSO phase. *Aust. Meteor. Mag.,* **43,** 205–212.

Yamagata, T., S. K. Behera, S. A. Rao, Z. Guan, K. Ashok, and H. N. Saji, 2003: Comments on ''Dipoles, temperature gradients, and tropical climate anomalies.'' *Bull. Amer. Meteor. Soc.,* **84,** 1418–1422, doi:10.1175/BAMS-84-10-1418.

Zanchettin, D., O. Bothe, W. Müller, J. Bader, and J. Jungclaus, 2014: Different flavors of the Atlantic multidecadal variability. *Climate Dyn.,* **42,** 381–399, doi:10.1007/s00382-013-1669-0.